

First measurement of the CKM angle ϕ_3 with $B^\pm \rightarrow D(K_S^0 \pi^+ \pi^- \pi^0) K^\pm$ decays

The Belle Collaboration

P. K. Resmi,^{21,†} J. Libby,²¹ K. Trabelsi,³⁷ I. Adachi,^{13,10} H. Aihara,⁷⁹ S. Al Said,^{74,31}
 D. M. Asner,² V. Aulchenko,^{3,60} T. Aushev,⁴⁹ V. Babu,⁶ I. Badhrees,^{74,30}
 A. M. Bakich,⁷³ C. Beleño,⁹ J. Bennett,⁴⁶ V. Bhardwaj,¹⁷ B. Bhuyan,¹⁹ T. Bilka,⁴
 J. Biswal,²⁷ A. Bozek,⁵⁷ M. Bračko,^{43,27} M. Campajola,^{24,52} D. Červenkov,⁴
 A. Chen,⁵⁴ B. G. Cheon,¹¹ H. E. Cho,¹¹ K. Cho,³³ Y. Choi,⁷² S. Choudhury,²⁰
 D. Cinabro,⁸³ S. Cunliffe,⁶ N. Dash,¹⁸ G. De Nardo,^{24,52} F. Di Capua,^{24,52}
 S. Di Carlo,³⁷ Z. Doležal,⁴ T. V. Dong,⁸ S. Eidelman,^{3,60,39} D. Epifanov,^{3,60}
 J. E. Fast,⁶² T. Ferber,⁶ B. G. Fulsom,⁶² R. Garg,⁶³ V. Gaur,⁸² N. Gabyshev,^{3,60}
 A. Garmash,^{3,60} A. Giri,²⁰ P. Goldenzweig,²⁸ B. Golob,^{40,27} Y. Guan,⁵ K. Hayasaka,⁵⁹
 H. Hayashii,⁵³ W.-S. Hou,⁵⁶ K. Huang,⁵⁶ T. Iijima,^{51,50} K. Inami,⁵⁰ G. Inguglia,²³
 A. Ishikawa,^{13,10} R. Itoh,^{13,10} M. Iwasaki,⁶¹ Y. Iwasaki,¹³ W. W. Jacobs,²²
 H. B. Jeon,³⁶ Y. Jin,⁷⁹ D. Joffe,²⁹ A. B. Kaliyar,²¹ K. H. Kang,³⁶ G. Karyan,⁶
 T. Kawasaki,³² C. Kiesling,⁴⁴ D. Y. Kim,⁷¹ K. T. Kim,³⁴ S. H. Kim,¹¹ K. Kinoshita,⁵
 P. Kodyš,⁴ D. Kotchetkov,¹² P. Krizan,^{40,27} R. Kroeger,⁴⁶ P. Krokovny,^{3,60} T. Kuhr,⁴¹
 R. Kumar,⁶⁶ A. Kuzmin,^{3,60} Y.-J. Kwon,⁸⁵ S. C. Lee,³⁶ Y. B. Li,⁶⁴ K. Lieret,⁴¹
 D. Liventsev,^{82,13} P.-C. Lu,⁵⁶ T. Luo,⁸ C. MacQueen,⁴⁵ M. Masuda,⁷⁸ T. Matsuda,⁴⁷
 D. Matvienko,^{3,60,39} M. Merola,^{24,52} K. Miyabayashi,⁵³ R. Mizuk,^{39,49}
 G. B. Mohanty,⁷⁵ H. K. Moon,³⁴ T. Nakano,⁶⁷ M. Nakao,^{13,10} K. J. Nath,¹⁹
 M. Nayak,^{83,13} M. Niiyama,³⁵ N. K. Nisar,⁶⁵ S. Nishida,^{13,10} K. Nishimura,¹²
 S. Ogawa,⁷⁶ H. Ono,^{58,59} Y. Onuki,⁷⁹ P. Pakhlov,^{39,48} G. Pakhlova,^{39,49} B. Pal,²
 S. Pardi,²⁴ H. Park,³⁶ T. K. Pedlar,⁴² R. Pestotnik,²⁷ L. E. Piilonen,⁸² E. Prencipe,¹⁵
 M. T. Prim,²⁸ M. Ritter,⁴¹ M. Röhrken,⁶ G. Russo,⁵² D. Sahoo,⁷⁵ Y. Sakai,^{13,10}
 S. Sandilya,⁵ L. Santelj,¹³ T. Sanuki,⁷⁷ V. Savinov,⁶⁵ O. Schneider,³⁸ G. Schnell,^{1,16}
 C. Schwanda,²³ A. J. Schwartz,⁵ Y. Seino,⁵⁹ K. Senyo,⁸⁴ M. E. Seviar,⁴⁵
 V. Shebalin,¹² C. P. Shen,⁸ J.-G. Shiu,⁵⁶ B. Shwartz,^{3,60} E. Solovieva,³⁹ M. Starič,²⁷
 Z. S. Stottler,⁸² J. F. Strube,⁶² T. Sumiyoshi,⁸¹ M. Takizawa,^{70,14,68} U. Tamponi,²⁵
 K. Tanida,²⁶ F. Tenchini,⁶ M. Uchida,⁸⁰ T. Uglov,^{39,49} S. Uno,^{13,10} Y. Usov,^{3,60}
 R. Van Tonder,²⁸ G. Varner,¹² A. Vinokurova,^{3,60} V. Vorobyev,^{3,60,39} A. Vossen,⁷
 B. Wang,⁴⁴ C. H. Wang,⁵⁵ M.-Z. Wang,⁵⁶ X. L. Wang,⁸ S. Watanuki,⁷⁷ E. Won,³⁴
 S. B. Yang,³⁴ H. Ye,⁶ Z. P. Zhang,⁶⁹ V. Zhilich,^{3,60} and V. Zhukova³⁹

[†]Corresponding author.

- ¹*University of the Basque Country UPV/EHU, 48080 Bilbao, Spain*
- ²*Brookhaven National Laboratory, Upton, New York 11973, USA*
- ³*Budker Institute of Nuclear Physics SB RAS, Novosibirsk 630090, Russian Federation*
- ⁴*Faculty of Mathematics and Physics, Charles University, 121 16 Prague, The Czech Republic*
- ⁵*University of Cincinnati, Cincinnati, OH 45221, USA*
- ⁶*Deutsches Elektronen-Synchrotron, 22607 Hamburg, Germany*
- ⁷*Duke University, Durham, NC 27708, USA*
- ⁸*Key Laboratory of Nuclear Physics and Ion-beam Application (MOE) and Institute of Modern Physics, Fudan University, Shanghai 200443, PR China*
- ⁹*II. Physikalisches Institut, Georg-August-Universität Göttingen, 37073 Göttingen, Germany*
- ¹⁰*SOKENDAI (The Graduate University for Advanced Studies), Hayama 240-0193, Japan*
- ¹¹*Department of Physics and Institute of Natural Sciences, Hanyang University, Seoul 04763, South Korea*
- ¹²*University of Hawaii, Honolulu, HI 96822, USA*
- ¹³*High Energy Accelerator Research Organization (KEK), Tsukuba 305-0801, Japan*
- ¹⁴*J-PARC Branch, KEK Theory Center, High Energy Accelerator Research Organization (KEK), Tsukuba 305-0801, Japan*
- ¹⁵*Forschungszentrum Jülich, 52425 Jülich, Germany*
- ¹⁶*IKERBASQUE, Basque Foundation for Science, 48013 Bilbao, Spain*
- ¹⁷*Indian Institute of Science Education and Research Mohali, SAS Nagar, 140306, India*
- ¹⁸*Indian Institute of Technology Bhubaneswar, Satya Nagar 751007, India*
- ¹⁹*Indian Institute of Technology Guwahati, Assam 781039, India*
- ²⁰*Indian Institute of Technology Hyderabad, Telangana 502285, India*
- ²¹*Indian Institute of Technology Madras, Chennai 600036, India*
- ²²*Indiana University, Bloomington, IN 47408, USA*
- ²³*Institute of High Energy Physics, Vienna 1050, Austria*
- ²⁴*INFN - Sezione di Napoli, 80126 Napoli, Italy*
- ²⁵*INFN - Sezione di Torino, 10125 Torino, Italy*
- ²⁶*Advanced Science Research Center, Japan Atomic Energy Agency, Naka 319-1195, Japan*
- ²⁷*J. Stefan Institute, 1000 Ljubljana, Slovenia*
- ²⁸*Institut für Experimentelle Teilchenphysik, Karlsruher Institut für Technologie, 76131 Karlsruhe, Germany*
- ²⁹*Kennesaw State University, Kennesaw GA 30144, USA*
- ³⁰*King Abdulaziz City for Science and Technology, Riyadh 11442, Saudi Arabia*
- ³¹*Department of Physics, Faculty of Science, King Abdulaziz University, Jeddah 21589, Saudi Arabia*
- ³²*Kitasato University, Sagami-hara 252-0373, Japan*
- ³³*Korea Institute of Science and Technology Information, Daejeon 34141, South Korea*
- ³⁴*Korea University, Seoul 02841, South Korea*
- ³⁵*Kyoto University, Kyoto 606-8502, Japan*
- ³⁶*Kyungpook National University, Daegu 41566, South Korea*
- ³⁷*LAL, Univ. Paris-Sud, CNRS/IN2P3, Université Paris-Saclay, Orsay 91898, France*
- ³⁸*École Polytechnique Fédérale de Lausanne (EPFL), Lausanne 1015, Switzerland*

- ³⁹*P.N. Lebedev Physical Institute of the Russian Academy of Sciences, Moscow 119991, Russian Federation*
- ⁴⁰*Faculty of Mathematics and Physics, University of Ljubljana, 1000 Ljubljana, Slovenia*
- ⁴¹*Ludwig Maximilians University, 80539 Munich, Germany*
- ⁴²*Luther College, Decorah, IA 52101, USA*
- ⁴³*University of Maribor, 2000 Maribor, Slovenia*
- ⁴⁴*Max-Planck-Institut für Physik, 80805 München, Germany*
- ⁴⁵*School of Physics, University of Melbourne, Victoria 3010, Australia*
- ⁴⁶*University of Mississippi, University, MS 38677, USA*
- ⁴⁷*University of Miyazaki, Miyazaki 889-2192, Japan*
- ⁴⁸*Moscow Physical Engineering Institute, Moscow 115409, Russian Federation*
- ⁴⁹*Moscow Institute of Physics and Technology, Moscow Region 141700, Russian Federation*
- ⁵⁰*Graduate School of Science, Nagoya University, Nagoya 464-8602, Japan*
- ⁵¹*Kobayashi-Maskawa Institute, Nagoya University, Nagoya 464-8602, Japan*
- ⁵²*Università di Napoli Federico II, 80055 Napoli, Italy*
- ⁵³*Nara Women's University, Nara 630-8506, Japan*
- ⁵⁴*National Central University, Chung-li 32054, Taiwan*
- ⁵⁵*National United University, Miao Li 36003, Taiwan*
- ⁵⁶*Department of Physics, National Taiwan University, Taipei 10617, Taiwan*
- ⁵⁷*H. Niewodniczanski Institute of Nuclear Physics, Krakow 31-342, Poland*
- ⁵⁸*Nippon Dental University, Niigata 951-8580, Japan*
- ⁵⁹*Niigata University, Niigata 950-2181, Japan*
- ⁶⁰*Novosibirsk State University, Novosibirsk 630090, Russian Federation*
- ⁶¹*Osaka City University, Osaka 558-8585, Japan*
- ⁶²*Pacific Northwest National Laboratory, Richland, WA 99352, USA*
- ⁶³*Panjab University, Chandigarh 160014, India*
- ⁶⁴*Peking University, Beijing 100871, PR China*
- ⁶⁵*University of Pittsburgh, Pittsburgh, PA 15260, USA*
- ⁶⁶*Punjab Agricultural University, Ludhiana 141004, India*
- ⁶⁷*Research Center for Nuclear Physics, Osaka University, Osaka 567-0047, Japan*
- ⁶⁸*Theoretical Research Division, Nishina Center, RIKEN, Saitama 351-0198, Japan*
- ⁶⁹*University of Science and Technology of China, Hefei 230026, PR China*
- ⁷⁰*Showa Pharmaceutical University, Tokyo 194-8543, Japan*
- ⁷¹*Soongsil University, Seoul 06978, South Korea*
- ⁷²*Sungkyunkwan University, Suwon 16419, South Korea*
- ⁷³*School of Physics, University of Sydney, New South Wales 2006, Australia*
- ⁷⁴*Department of Physics, Faculty of Science, University of Tabuk, Tabuk 71451, Saudi Arabia*
- ⁷⁵*Tata Institute of Fundamental Research, Mumbai 400005, India*
- ⁷⁶*Toho University, Funabashi 274-8510, Japan*
- ⁷⁷*Department of Physics, Tohoku University, Sendai 980-8578, Japan*
- ⁷⁸*Earthquake Research Institute, University of Tokyo, Tokyo 113-0032, Japan*
- ⁷⁹*Department of Physics, University of Tokyo, Tokyo 113-0033, Japan*
- ⁸⁰*Tokyo Institute of Technology, Tokyo 152-8550, Japan*
- ⁸¹*Tokyo Metropolitan University, Tokyo 192-0397, Japan*

⁸² *Virginia Polytechnic Institute and State University, Blacksburg, VA 24061, USA*

⁸³ *Wayne State University, Detroit, MI 48202, USA*

⁸⁴ *Yamagata University, Yamagata 990-8560, Japan*

⁸⁵ *Yonsei University, Seoul 03722, South Korea*

E-mail: resmipk@physics.iitm.ac.in

ABSTRACT: We present the first model-independent measurement of the CKM unitarity triangle angle ϕ_3 using $B^\pm \rightarrow D(K_S^0 \pi^+ \pi^- \pi^0) K^\pm$ decays, where D indicates either a D^0 or \bar{D}^0 meson. Measurements of the strong-phase difference of the $D \rightarrow K_S^0 \pi^+ \pi^- \pi^0$ amplitude obtained from CLEO-c data are used as input. This analysis is based on the full Belle data set of 772×10^6 $B\bar{B}$ events collected at the $\Upsilon(4S)$ resonance. We obtain $\phi_3 = (5.7^{+10.2}_{-8.8} \pm 3.5 \pm 5.7)^\circ$ and the suppressed amplitude ratio $r_B = 0.323 \pm 0.147 \pm 0.023 \pm 0.051$. Here the first uncertainty is statistical, the second is the experimental systematic, and the third is due to the precision of the strong-phase parameters measured from CLEO-c data. The 95% confidence interval on ϕ_3 is $(-29.7, 109.5)^\circ$, which is consistent with the current world average.

KEYWORDS: e^+e^- experiments, flavour physics, CP violation, Unitarity Triangle angle ϕ_3

Contents

1	Introduction	1
2	Formalism for measuring ϕ_3 with $B^+ \rightarrow D(K_S^0\pi^+\pi^-\pi^0)K^+$ decays	2
3	External measurements of c_i and s_i	4
4	Data samples and the Belle detector	5
5	Analysis Overview	6
5.1	Efficiency	7
5.2	Momentum resolution	7
5.3	Signal extraction	7
6	Event selection	8
7	Determination of K_i and \bar{K}_i from the D^{*+} sample	11
8	Determination of (x_{\pm}, y_{\pm}) from the $B^{\pm} \rightarrow Dh^{\pm}$ sample	12
9	Systematic uncertainties	17
10	Determination of ϕ_3, r_B and δ_B	19
11	Conclusion	21
A	Efficiency and Migration matrix	23

1 Introduction

The description of CP violation in the standard model (SM) can be tested via measurements of observables related to the Cabibbo-Kobayashi-Maskawa (CKM) matrix [1, 2]. One such test is the measurement of the unitarity-triangle angle $\phi_3 \equiv \arg(-V_{ud}V_{ub}^*/V_{cd}V_{cb}^*)$, also denoted as γ . Here, V_{ij} refers to the CKM matrix element. The angle ϕ_3 is accessible through tree-level amplitudes, and the associated theoretical uncertainty is negligible [$\mathcal{O}(10^{-7})$] [3]. A comparison of the direct measurements of ϕ_3 with the value inferred from other measurements related to the CKM matrix [4], which are more likely to be influenced by beyond-SM physics [5, 6], provides a probe for new physics. The current experimental uncertainty on ϕ_3 [4] limits such tests, motivating more precise measurements of the angle.

The measurement of ϕ_3 is possible when there is interference between the transitions $\bar{b} \rightarrow \bar{c}u\bar{s}$ and $\bar{b} \rightarrow \bar{u}c\bar{s}$. This is the case in the decay $B^+ \rightarrow DK^+$, where D is a neutral

charm meson decaying to a final state common to both D^0 and \bar{D}^0 . Here and elsewhere in this paper, inclusion of charge-conjugate final states is implied unless explicitly stated otherwise. Currently, the most precise measurement of ϕ_3 [7] exploits the self-conjugate final state $D \rightarrow K_S^0 \pi^+ \pi^-$, where the CP asymmetry in different regions of the D meson Dalitz plot is measured to determine ϕ_3 [8, 9]. The analysis requires knowledge of the strong-phase difference between the D^0 and \bar{D}^0 decay amplitudes, and measured values of the strong-phase differences averaged over Dalitz plot bins are used as input [10]. Given the success of such analyses in obtaining ϕ_3 [7, 11], other self-conjugate final states can be studied in a similar fashion to improve the determination of ϕ_3 .

In this paper, we present the first measurements of the decay $B^+ \rightarrow D(K_S^0 \pi^+ \pi^- \pi^0) K^+$ to determine ϕ_3 using the same formalism as with $B^+ \rightarrow D(K_S^0 \pi^+ \pi^-) K^+$ [8, 9]. The decay $D \rightarrow K_S^0 \pi^+ \pi^- \pi^0$ is a suitable addition because it has a branching fraction of 5.2% [12], which is large compared to that of other multibody final states including $K_S^0 \pi^+ \pi^-$. The decay occurs through many intermediate resonances, such as $K_S^0 \omega$ and $K^{*\pm} \rho^\mp$, that lead to variations of the strong-phase difference over the phase space, a requirement for extracting ϕ_3 from a single final state. However, a significant complication is that the four-body final state requires a binning of the five-dimensional D phase space, as opposed to a two-dimensional Dalitz plot for the three-body case. The measurement is performed with an e^+e^- collision data sample collected by the Belle detector at a centre-of-mass energy corresponding to the $\Upsilon(4S)$ resonance. The sample contains 772×10^6 $B\bar{B}$ events corresponding to an integrated luminosity of 711 fb^{-1} . As an input to the analysis, we use the strong-phase difference measurements in phase space bins [13] obtained from an analysis of CLEO-c [14–17] data ¹.

The remainder of this paper is arranged as follows. Section 2 describes the formalism of the method for measuring ϕ_3 . The inputs derived from CLEO-c data and the Belle data and detector are described in sections 3 and 4, respectively, after which an overview of the analysis strategy is presented, in section 5. The event selection criteria are given in section 6, and the signal yield determination in the flavour-tagged D sample, which is a required input to the analysis, is presented in section 7. The measurement of CP violation in the B sample in bins of the D phase space is explained in section 8 and the related systematic uncertainty estimation is listed in section 9. The extraction of the physics parameter ϕ_3 and the average of this result with previous Belle measurements are presented in section 10, before conclusions given in section 11.

2 Formalism for measuring ϕ_3 with $B^+ \rightarrow D(K_S^0 \pi^+ \pi^- \pi^0) K^+$ decays

The determination of ϕ_3 from $B^+ \rightarrow DK^+$ decays, where the D meson decays to a multibody self-conjugate final state, can be performed via two methods: model-dependent and -independent. The model-dependent method requires a model of the amplitudes describing

¹Normal activities of the CLEO Collaboration ceased in 2012. However, access to the data was still possible for former CLEO Collaboration members and several results have been published. Any such publication, such as ref. [13] are not official results of the CLEO Collaboration. Hence we refer to results from CLEO-c data rather than from the CLEO Collaboration.

the intermediate resonances and partial waves, assumed to be contributing to the decay, to be fitted to the distribution of events over the D phase space. Model assumptions used in the method lead to a difficult determination of systematic uncertainty and may limit the precision of the ϕ_3 measurement, to as much as $\pm 8\text{--}9^\circ$ [18]. On the other hand, the model-independent method requires that measurements of CP -violating asymmetries are made in distinct regions of D meson phase space, which we refer to as bins. The binning reduces the statistical precision compared to the model-dependent method, but the uncertainty related to model assumptions is removed by using independent measurements of the average strong-phase differences, bin-by-bin. The average strong-phase differences can be determined using e^+e^- collision data at the open-charm threshold, which has been done for $D^0 \rightarrow K_S^0\pi^+\pi^-\pi^0$ [13]. Therefore, given its systematic robustness, we follow the model-independent approach. We introduce the method in the remainder of this section.

The amplitude for the decay $B^+ \rightarrow DK^+$, $D \rightarrow f$, where f is a common multibody final state from the D^0 and \bar{D}^0 decay, can be written as

$$A_B = \bar{A} + r_B e^{i(\delta_B + \phi_3)} A, \quad (2.1)$$

where A is the amplitude for $D^0 \rightarrow f$ at a point in the allowed phase space \mathcal{D} , \bar{A} is the amplitude for $\bar{D}^0 \rightarrow f$ at the same point in phase space, r_B is the ratio of the absolute values of $B^+ \rightarrow \bar{D}^0 K^+$ and $B^+ \rightarrow D^0 K^+$ decay amplitudes, and δ_B is the strong-phase difference between the two $B \rightarrow DK$ amplitudes. Thus, the probability density for a decay at a point in \mathcal{D} is

$$P_B = |A_B|^2 = |\bar{A}|^2 + r_B^2 |A|^2 + 2r_B \Re \left[\bar{A}^* A e^{i(\delta_B + \phi_3)} \right]. \quad (2.2)$$

Furthermore,

$$\bar{A}^* A = |\bar{A}| |A| e^{i(\delta_D - \delta_{\bar{D}})} = |\bar{A}| |A| e^{i\Delta\delta_D}, \quad (2.3)$$

where δ_D and $\delta_{\bar{D}}$ are the strong phases for $D^0 \rightarrow f$ and $\bar{D}^0 \rightarrow f$ decays, respectively. With this, eq. 2.2 becomes

$$\begin{aligned} P_B &= |\bar{A}|^2 + r_B^2 |A|^2 + 2r_B |\bar{A}| |A| [\cos \Delta\delta_D \cos(\delta_B + \phi_3) - \sin \Delta\delta_D \sin(\delta_B + \phi_3)] \\ &= \bar{P} + r_B^2 P + 2\sqrt{P\bar{P}}(x_+ C - y_+ S), \end{aligned} \quad (2.4)$$

where $P = |A|^2$, $\bar{P} = |\bar{A}|^2$, $x_+ = r_B \cos(\delta_B + \phi_3)$, $y_+ = r_B \sin(\delta_B + \phi_3)$, $C = \cos \Delta\delta_D$ and $S = \sin \Delta\delta_D$. For the charge-conjugate mode, $B^- \rightarrow DK^-$, the density is given by the same expression, with $A \leftrightarrow \bar{A}$ and $\phi_3 \rightarrow -\phi_3$, which leads to the definitions $x_- = r_B \cos(\delta_B - \phi_3)$ and $y_- = r_B \sin(\delta_B - \phi_3)$. The partial decay rates for $B^\pm \rightarrow DK^\pm$ within the i^{th} bin of \mathcal{D} , which corresponds to a subset of phase space \mathcal{D}_i , are

$$\Gamma_i^- = h(K_i + r_B^2 \bar{K}_i + 2\sqrt{K_i \bar{K}_i}(c_i x_- + s_i y_-)), \quad (2.5)$$

$$\Gamma_i^+ = h(\bar{K}_i + r_B^2 K_i + 2\sqrt{K_i \bar{K}_i}(c_i x_+ - s_i y_+)), \quad (2.6)$$

where K_i and \bar{K}_i are the fractions of flavour-tagged D^0 and \bar{D}^0 events in \mathcal{D}_i and h is the common normalization factor. A sample of $D^0 \rightarrow K_S^0\pi^+\pi^-\pi^0$ candidates from $D^{*+} \rightarrow$

$D^0\pi^+$ decays, where the charge of the pion from the D^{*+} decay tags the flavour of the D meson, are used to determine values of K_i and \bar{K}_i . The c_i and s_i parameters are the amplitude-weighted averages of C and S over the region \mathcal{D}_i . The c_i parameter is defined as

$$c_i = \frac{\int_{\mathcal{D}_i} \sqrt{P\bar{P}} C d\mathcal{D}}{\sqrt{\int_{\mathcal{D}_i} P d\mathcal{D} \int_{\mathcal{D}_i} \bar{P} d\mathcal{D}}}, \quad (2.7)$$

and the definition of s_i is the same, with C being replaced by S . Therefore, with c_i , s_i , K_i , and \bar{K}_i given as external inputs to the analysis, one can determine x_{\pm} , y_{\pm} and h from a set of partial decay rate measurements, when \mathcal{D} is divided into three or more bins. The loss of statistical precision can be mitigated by increasing the number of bins; with an increased number of bins, however, the uncertainty on the external inputs also increases, limiting the precision of the measurement. The method by which the values of x_{\pm} and y_{\pm} are used to constrain ϕ_3 , r_B and δ_B is described in section 10.

3 External measurements of c_i and s_i

The values of c_i and s_i for the decay $D \rightarrow K_S^0\pi^+\pi^-\pi^0$ have been determined using e^+e^- collision data collected at a centre-of-mass energy corresponding to the $\psi(3770)$ resonance [13]. The quantum correlations between the neutral D mesons produced in decays of the $\psi(3770)$ are exploited to extract the strong-phase differences in bins of the phase space. This four-body final state has a five-dimensional phase space, which was divided into nine exclusive bins, selected to contain different intermediate resonances, thus minimizing the strong-phase variation within the bin as much as possible. The sensitivity of the binning could be improved upon using an amplitude model of $D^0 \rightarrow K_S^0\pi^+\pi^-\pi^0$, which is unavailable at present. The binning scheme is listed in table 1. In each successive bin, only events that do not belong to the previous bins are selected (e.g. bin 2 is populated by events with $m_{K_S^0\pi^-}$ and $m_{\pi^+\pi^0}$ within the denoted intervals, and $m_{\pi^+\pi^-\pi^0}$ not in the denoted interval for bin 1). The bins are thus exclusive.

Certain constraints are imposed in the fit, which arise from the nature of the symmetry between the bins, to extract c_i and s_i parameters. Bins 1, 6 and 9 are CP self-conjugate, which implies

$$s_1 = 0, \quad s_6 = 0, \quad s_9 = 0. \quad (3.1)$$

Bin 9 is CP self-conjugate because the region corresponding to the sum of bins 1 to 8 is CP self-conjugate. Bins 2 and 3, 4 and 5, and 7 and 8 are pairwise CP -conjugate, which imposes a relation between their s_i values:

$$s_i \sqrt{K_i \bar{K}_i} + s_{i+1} \sqrt{K_{i+1} \bar{K}_{i+1}} = 0, \quad (3.2)$$

where $i = 2, 4$ and 7 . The results for c_i and s_i are summarized in table 2 and are shown in figure 1. In the analysis we use the same binning scheme so that c_i and s_i can be taken as external inputs in determining x_{\pm} and y_{\pm} .

Bin no.	Bin region	m_L (GeV/ c^2)	m_U (GeV/ c^2)
1	$m_{\pi^+\pi^-\pi^0} \approx m_\omega$	0.762	0.802
2	$m_{K_S^0\pi^-} \approx m_{K^{*-}}$	0.790	0.994
	$m_{\pi^+\pi^0} \approx m_{\rho^+}$	0.610	0.960
3	$m_{K_S^0\pi^+} \approx m_{K^{*+}}$	0.790	0.994
	$m_{\pi^-\pi^0} \approx m_{\rho^-}$	0.610	0.960
4	$m_{K_S^0\pi^-} \approx m_{K^{*-}}$	0.790	0.994
5	$m_{K_S^0\pi^+} \approx m_{K^{*+}}$	0.790	0.994
6	$m_{K_S^0\pi^0} \approx m_{K^{*0}}$	0.790	0.994
7	$m_{\pi^+\pi^0} \approx m_{\rho^+}$	0.610	0.960
8	$m_{\pi^-\pi^0} \approx m_{\rho^-}$	0.610	0.960
9	Remainder	-	-

Table 1. Specifications of the nine exclusive bins of $D \rightarrow K_S^0\pi^+\pi^-\pi^0$ phase space. Here m_L and m_U are the lower and upper limit, respectively, of the invariant mass in each region [13].

Bin no.	c_i	s_i
1	$-1.11 \pm 0.09_{-0.01}^{+0.02}$	0.00
2	$-0.30 \pm 0.05 \pm 0.01$	$-0.03 \pm 0.09_{-0.02}^{+0.01}$
3	$-0.41 \pm 0.07_{-0.01}^{+0.02}$	$0.04 \pm 0.12_{-0.02}^{+0.01}$ *
4	$-0.79 \pm 0.09 \pm 0.05$	$-0.44 \pm 0.18 \pm 0.06$
5	$-0.62 \pm 0.12_{-0.02}^{+0.03}$	$0.42 \pm 0.20 \pm 0.06$ *
6	$-0.19 \pm 0.11 \pm 0.02$	0.00
7	$-0.82 \pm 0.11 \pm 0.03$	$-0.11 \pm 0.19_{-0.03}^{+0.04}$
8	$-0.63 \pm 0.18 \pm 0.03$	$0.23 \pm 0.41_{-0.03}^{+0.04}$ *
9	$-0.69 \pm 0.15_{-0.12}^{+0.15}$	0.00

Table 2. Values of c_i and s_i reported in ref. [13]. The uncertainties are statistical and systematic, respectively. The s_i results marked by * in bins 3, 5 and 8 are derived from those in other bins, according to the constraints of eq. (3.2). The statistical uncertainty on these s_i values include contribution from K_i values according to the error propagation formalism.

4 Data samples and the Belle detector

We use an e^+e^- collision data sample containing 772×10^6 $B\bar{B}$ events collected by the Belle detector at a centre-of-mass energy corresponding to the pole of the $\Upsilon(4S)$ resonance. Monte Carlo (MC) simulated samples are used to optimize the selection, determine selection efficiencies, and identify sources of background. The MC samples of signal and background processes are generated using EvtGen [19] with the GEANT [20] package being subsequently used to model the detector response to the decay products. PHOTOS [21] incorporates effects due to final-state radiation from charged particles.

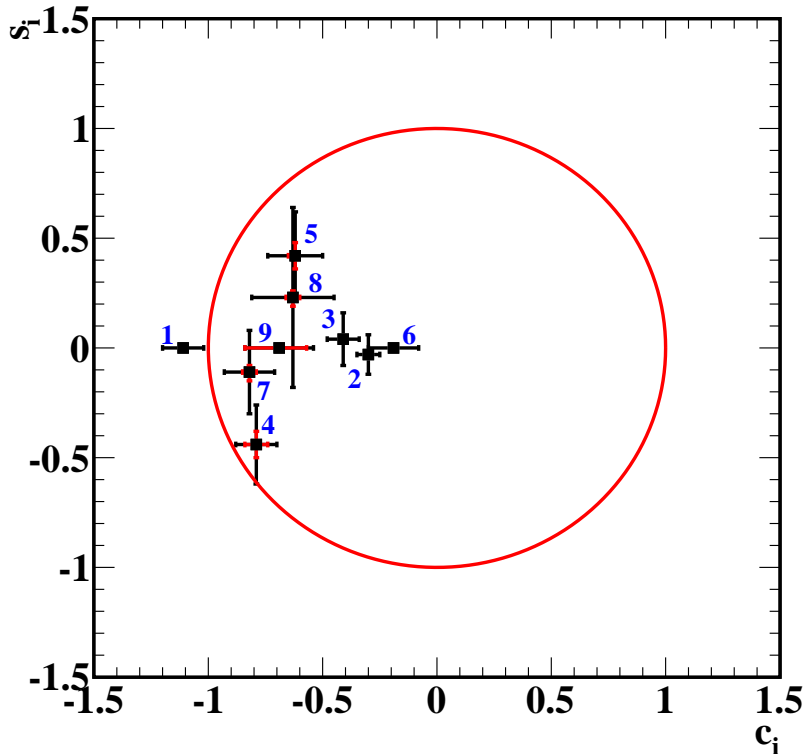


Figure 1. Values of c_i and s_i reported in ref. [13]. The black and red error bars represent statistical and systematic uncertainties, respectively.

The Belle detector [22, 23] was located at the interaction point of the KEKB asymmetric-energy e^+e^- collider [24, 25]. The detector subsystems relevant for this study are: the silicon vertex detector (SVD) and central drift chamber (CDC), for charged particle tracking and measurement of energy loss due to ionization (dE/dx); the aerogel threshold Cherenkov counters (ACC) and time-of-flight (TOF) scintillation counters, for particle identification (PID); and the electromagnetic calorimeter (ECL) consisting of an array of CsI(Tl) crystals to measure photon energies. These subsystems are situated in a magnetic field of 1.5 T. A more detailed description of the Belle detector can be found in refs. [22, 23].

5 Analysis Overview

The essence of the analysis lies in eqs. (2.5) and (2.6), which describe the partial decay rates in each bin. However, these relations do not account for experimental resolution and acceptance. For example, the invariant mass resolution causes events to be assigned to bins outside of their origin, an effect we shall call “migration”. The background contributions are to be considered as well. Here we briefly summarize how these experimental effects are accounted for.

5.1 Efficiency

Three different samples are used in this analysis, each with differing selection efficiencies due to the kinematic differences between the final states: the quantum correlated $D\bar{D}$ sample from $\psi(3770)$ decays, the Belle sample of $B^+ \rightarrow Dh^+$, where $h = (K, \pi)$, and the Belle sample of $D^{*+} \rightarrow D\pi^+$ used to determine K_i and \bar{K}_i . The sample of $B^+ \rightarrow D\pi^+$ is used as a control sample, as it is topologically identical to the signal, but with negligible expected CP violation [26]. The c_i and s_i results measured with CLEO-c data have been corrected for efficiency. Efficiency variation among bins will not matter if the efficiency profile is the same for both $B^+ \rightarrow Dh^+$ and flavour-tagged D samples. This is partially achieved by requiring similar kinematic properties for the D meson in both samples. The efficiency profile depends primarily on D momentum, hence we select the flavour-tagged D sample in such a way that the D momentum approximately matches that of the $B^+ \rightarrow Dh^+$ sample. The matching is not exact, so independent efficiency corrections are applied to the yields in both samples while calculating the parameters of interest.

5.2 Momentum resolution

The finite momentum resolution causes events to migrate among the bins. The c_i and s_i results are obtained after applying corrections for these migration effects. The amount of migration in both B and D^* samples is estimated as a migration matrix M_{ij} . The matrix has its diagonal elements close to one, and off-diagonal elements are small. MC samples of signal events are used to obtain the migration matrix. The data yield in each bin, Y_i , is modified as $Y'_i = M_{ij}Y_j$. Any difference between the invariant mass resolution in the data and MC samples must be taken into account. We find the effect of the difference in resolution is only significant in bin 1, which contains the ω resonance. This bin is narrow due to the small natural width of the ω . However, the natural width is the same order as the $m_{\pi^+\pi^-\pi^0}$ resolution, so there is significant migration out of this bin that is not compensated by migration into bin 1. Therefore, the M_{1j} elements of the migration matrix are determined after applying a Gaussian smearing to the value of $m_{\pi^+\pi^-\pi^0}$ by a scale factor. The scale factor is obtained from the observed difference in ω mass resolution between data and MC samples. The scale factors are 1.13 ± 0.02 and 1.09 ± 0.02 for the $B^+ \rightarrow Dh^+$ and $D^{*+} \rightarrow D\pi^+$ samples, respectively.

5.3 Signal extraction

It is important to account for the background contributions in the sample while extracting the specified parameters. An extended maximum likelihood fit is performed on the data in each bin of the flavour-tagged D sample to extract the values of K_i and \bar{K}_i . The fit to the B sample in the bins of D phase space is performed using an extended likelihood fit that simultaneously fits all bins in the $B^+ \rightarrow DK^+$ and $B^+ \rightarrow D\pi^+$ decay modes, so that the values of the parameters x_{\pm} and y_{\pm} that are common to the expectation for each bin yield, can be extracted, as well as the cross-feed between these samples.

6 Event selection

We reconstruct the decays $B^+ \rightarrow DK^+$ and $B^+ \rightarrow D\pi^+$, where the neutral D meson decays to the four-body final state of $K_S^0\pi^+\pi^-\pi^0$. In addition, $D^{*+} \rightarrow D^0\pi^+$ decays produced via the $e^+e^- \rightarrow c\bar{c}$ continuum process are selected to determine the K_i and \bar{K}_i parameters.

For charged particle candidates originating directly from the B and D decays, we require that the track be within 0.5 cm and ± 3.0 cm of the interaction point (IP) in the directions perpendicular to (radial) and parallel to the z -axis, respectively; the z -axis is defined to be opposite to the e^+ beam direction. The charged tracks are classified as pions or kaons based on information from CDC, ACC, and TOF sub-detector systems. The pion (kaon) identification efficiency is 92% (84%) and the probability of misidentification as a kaon (pion) is 15% (8%) [27].

We select K_S^0 candidates from two oppositely charged tracks assumed to be pions. The invariant mass of the two tracks is required to be within the range 0.487–0.508 GeV/ c^2 corresponding to $\pm 3\sigma$ of the known K_S^0 mass [12], where σ is the mass resolution. A neural network [28] based selection is applied on the daughter tracks to remove background from random combinations [29]. The input variables to the neural network are the K_S^0 momentum in the lab frame, the distance between the two track helices along the z -axis at their point of closest approach, the K_S^0 flight length in the radial direction, the angle between the K_S^0 momentum and the vector joining the IP to the K_S^0 decay vertex, the angle between pion momentum and the boost direction of lab frame in K_S^0 rest frame and pion momentum in K_S^0 rest frame, the distances of closest approach in the radial direction between IP and the two pion helices, the number of hits in CDC for each pion track, and the presence of hits in the SVD for each pion track. The K_S^0 selection efficiency is 87%, which is determined from an MC sample of generic $B\bar{B}$ events.

The π^0 candidates are reconstructed from pairs of photons detected in the ECL. We select candidates with diphoton invariant mass M_{π^0} in the range 0.119–0.148 GeV/ c^2 , which corresponds to 3σ about the nominal π^0 mass [12]. The photon energy thresholds are optimized separately for π^0 candidates detected in combinations of the barrel, forward endcap (FWD EC) and backward endcap (BWD EC) regions of the ECL as given in table 3 by maximizing the significance $S/\sqrt{S+B}$, where S and B are the number of signal and background events selected from MC samples in the signal region, respectively. (The criteria that define the signal region are described later in this section.) Studies of MC samples indicate that candidates in the other ECL sector combinations make up only 1.5% of the total, and a common energy threshold of 50 MeV is applied on these. All selected combinations of $K_S^0\pi^+\pi^-\pi^0$ candidates are retained for further study. In addition, kinematic constraints are applied to the K_S^0 , π^0 , and D invariant masses and decay vertices to improve the momentum resolution of the B candidates, as well as the invariant masses used to bin the D phase space.

The $D^{*+} \rightarrow D^0\pi^+$ decay uses the charge of the accompanying pion to identify the flavour of the D meson. This pion is referred to as a slow pion because of the limited phase space of the decay that results in it having lower momentum on average than other final-state particles. To improve the momentum resolution of the slow pion, it is required

γ_1	γ_2	E_{γ_1} (MeV)	E_{γ_2} (MeV)
Barrel	Barrel	70	65
FWD EC	Barrel	220	65
Barrel	BWD EC	65	95
FWD EC	FWD EC	150	210

Table 3. Optimized E_γ thresholds for the photon candidates. The FWD EC, barrel, and BWD EC regions of the ECL are defined in the polar angle ranges $(12.4^\circ, 31.4^\circ)$, $(32.2^\circ, 128.7^\circ)$, and $(130.7^\circ, 155.1^\circ)$, respectively.

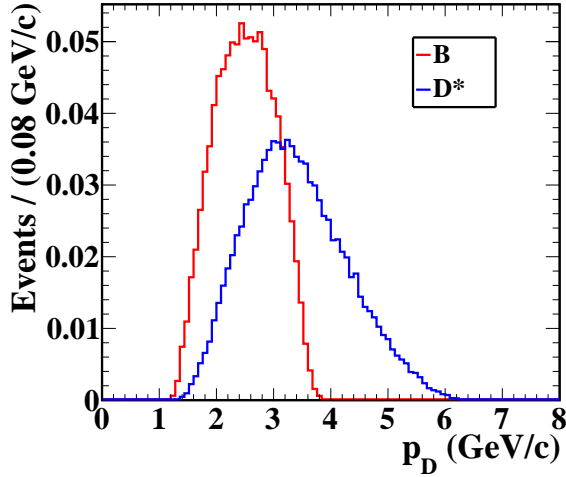


Figure 2. Distributions of the measured D meson momenta p_D in the lab frame for (blue) D^{*+} and (red) $B^+ \rightarrow Dh^+$ signal MC samples.

to have at least one hit in the SVD. Signal D^{*+} candidates are identified by two kinematic variables: M_D , the invariant mass of the D candidate, and ΔM , the difference in the invariant masses of D^{*+} and D meson candidates. The events that satisfy the criteria, $1.80 < M_D < 1.95 \text{ GeV}/c^2$ and $\Delta M < 0.15 \text{ GeV}/c^2$ are retained. The D meson momentum in the lab frame is chosen to be in the range 1–4 GeV/c to approximately match the range of D momentum in the $B^+ \rightarrow Dh^+$ sample, as illustrated in figure 2.

The D and π^+ candidates are constrained to come from a common vertex to form the D^{*+} candidate. On average, there are 1.6 D^{*+} candidates in an event. If there is more than one candidate in an event, the candidate with the smallest χ^2 value from the D^{*+} vertex fit is retained. This criterion selects the correct signal candidate in 69% of the events with multiple candidates. The overall selection efficiency is 3.7%, which includes the secondary branching fraction of $K_S^0 \rightarrow \pi^+\pi^-$.

A D candidate is combined with a charged kaon (pion) track to form a $B^+ \rightarrow DK^+$ ($B^+ \rightarrow D\pi^+$) candidate. The invariant mass of the D candidate is required to be in the range 1.835–1.890 GeV/c^2 . The signal candidates are identified using two kinematic variables, the energy difference ΔE and beam-energy-constrained mass M_{bc} , which are

defined as $\Delta E = E_B - E_{\text{beam}}$ and $M_{bc} = c^{-2} \sqrt{E_{\text{beam}}^2 - |\vec{\mathbf{p}}_B|^2 c^2}$, where E_B ($\vec{\mathbf{p}}_B$) is the energy (momentum) of the B candidate and E_{beam} is the beam energy in the centre-of-mass frame. We select candidates that satisfy the criteria $M_{bc} > 5.27 \text{ GeV}/c^2$ and $-0.13 < \Delta E < 0.30 \text{ GeV}$. The asymmetric ΔE window is chosen to avoid the peaking structure appearing at lower values from partially reconstructed $B^+ \rightarrow D^{(*)}K^{(*)+}$ decays. The signal region used while performing optimization of the selection is $|\Delta E| < 0.05 \text{ GeV}$. The average B candidate multiplicity is 1.3. In events with more than one candidate, we retain the candidate with the smallest value of $(\frac{M_{bc} - M_B^{\text{PDG}}}{\sigma_{M_{bc}}})^2 + (\frac{M_D - M_D^{\text{PDG}}}{\sigma_{M_D}})^2 + (\frac{M_{\pi^0} - M_{\pi^0}^{\text{PDG}}}{\sigma_{M_{\pi^0}}})^2$. Here, the masses M_i^{PDG} are those reported by the Particle Data Group [12] and the resolutions $\sigma_{M_{bc}}$, σ_{M_D} , and $\sigma_{M_{\pi^0}}$ are obtained from MC simulated samples of signal events. The best candidate selection criterion is 80% efficient in selecting the correctly reconstructed candidate.

The background from $e^+e^- \rightarrow q\bar{q}$ ($q = u, d, s, c$) continuum processes is suppressed by exploiting the difference in event topology compared to $e^+e^- \rightarrow \Upsilon(4S) \rightarrow B\bar{B}$ events. The continuum events are jet-like in nature, whereas $B\bar{B}$ events have a spherical topology, due to the low momentum of the B mesons produced via the $\Upsilon(4S)$ resonance. A neural-network-based algorithm [28] is used to discriminate between continuum background and B events. We also use variables related to the displaced vertices of B decays from the IP and the associated leptons/kaons from the non-signal B meson in the event, which give an additional handle to distinguish continuum events.

The eight input variables to the neural network are the likelihood ratio obtained via Fisher discriminants [30] formed from modified Fox-Wolfram moments [31, 32], the absolute value of the cosine of the angle between the B candidate and the z axis in the e^+e^- centre-of-mass frame, the absolute value of the cosine of the angle between the thrust axis of the B candidate and that of the rest of the event in the centre-of-mass frame, the vertex separation between the two B candidates [33] along z -axis, the absolute value of the B flavour-dilution factor [34], the difference between the sum of the charges of particles in the hemisphere about the D direction in the centre-of-mass frame and the one in the opposite hemisphere, excluding the particles used for the reconstruction of B , the product of the charge of the B and the sum of the charges of all kaons not used for reconstruction of B , and the cosine of the angle between the D direction and the direction opposite to that of the $\Upsilon(4S)$ in the B rest frame.

Signal and continuum MC samples are used to train the neural network. We require the neural network output, C_{NN} , to be greater than -0.6 , which reduces the continuum background by 67% with a loss of only 5% of the signal. The overall selection efficiency is 4.7% and 5.3% for $B^+ \rightarrow DK^+$ and $B^+ \rightarrow D\pi^+$ decays, respectively. These efficiencies include the secondary branching fraction of $K_S^0 \rightarrow \pi^+\pi^-$. The efficiencies in each bin and the migration matrix for the $B^+ \rightarrow Dh^+$ selection are given in appendix A.

7 Determination of K_i and \overline{K}_i from the D^{*+} sample

The fractions of D^0 and \overline{D}^0 events in each D phase space bin, represented as K_i and \overline{K}_i , are measured from the selected sample of $D^{*+} \rightarrow D\pi^+$ candidates. The yield of signal events is obtained from a two-dimensional unbinned extended maximum-likelihood fit to the distribution of M_D and ΔM for the selected candidates. The fit is performed independently in each bin. In general, there are two types of background: *combinatorial*, which is due to the random combination of final-state particles to form a D^{*+} candidate, and *random-slow-pion*, in which a correctly reconstructed D meson combines with a π^+ , which is not from a common D^{*+} decay, to form a candidate. The combinatorial background peaks neither in the M_D nor ΔM distributions, whereas the random-slow-pion background peaks only in the M_D distribution.

The signal component of the M_D distribution is described by a probability density function (PDF) that is the sum of a Crystal Ball (CB) [35] function and two Gaussian functions with a common mean. The combinatorial background PDF is parametrized by a first-order polynomial. The signal PDF is also used to model the random-slow-pion background distribution in M_D . The ΔM signal PDF is described by the sum of an asymmetric Gaussian and three Gaussian functions with a common mean. The combinatorial background ΔM distribution is parametrized by the sum of a threshold function and two Gaussian PDFs. The threshold function is

$$f(\Delta M) = (\Delta M - m_\pi)^{\frac{1}{2}} + \alpha(\Delta M - m_\pi)^{\frac{3}{2}} + \beta(\Delta M - m_\pi)^{\frac{5}{2}}, \quad (7.1)$$

where m_π is the mass of a charged pion [12], and α and β are shape parameters. In the final fit to data, the shape parameters are fixed to the values obtained from MC. The Gaussian functions describe a small peak in the ΔM combinatorial distribution, which is due to misreconstructed π^0 candidates. The parameters of the Gaussian functions and the fraction of candidates in the peak are fixed to the values obtained from a MC sample. The random-slow-pion background PDF is the same as the threshold function used to describe the combinatorial background.

The signal M_D and ΔM PDFs are correlated such that the width of the ΔM distribution depends upon M_D . The width of the core Gaussian in the ΔM signal PDF is parametrized as

$$\sigma(\Delta M) = a_0 + a_2(M_D - M_D^{\text{PDG}})^2, \quad (7.2)$$

where a_0 and a_2 are parameters to be determined from data. The correlation between M_D and ΔM distributions is found to be negligible in studies of background MC samples. Therefore, the one-dimensional PDFs are multiplied to obtain the total background PDF.

The yields, except that describing the peaking component in the combinatorial background ΔM distribution and the shape parameters $a_{0(2)}$, as well as the means of the signal in both M_D and ΔM are floated in the fit; all other parameters are fixed to the values obtained from fits to the corresponding MC sample. In each bin, the fit is performed simultaneously for D^0 and \overline{D}^0 categories to obtain the signal yield. Figure 3 shows the fit projections compared to the data within bin 1. These projections are signal-enhanced by

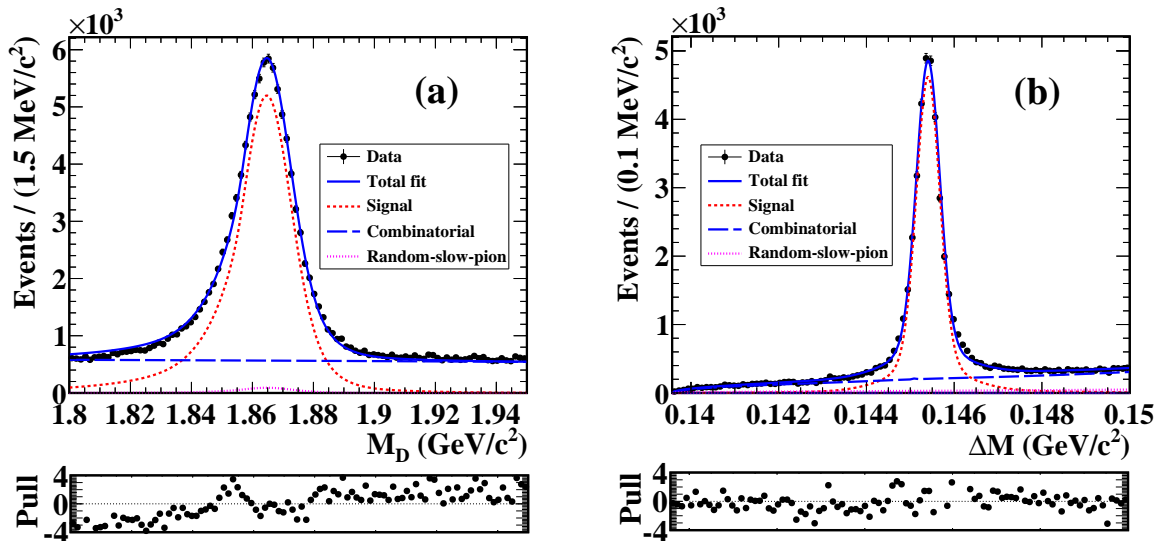


Figure 3. Signal-enhanced fit projections of (a) M_D and (b) ΔM distributions from $D^{*\pm} \rightarrow D\pi^\pm$ data sample in bin 1. The black points with error bars are the data and the solid blue curves show the total fit. The error bars are barely visible as they are smaller than the size of the points. The dotted red, blue and magenta curves represent the signal, combinatorial and random-slow-pion backgrounds, respectively. The pull between the fit and the data is shown below the distributions.

considering events in the signal region of the variable that is not plotted; the signal regions are defined as $1.86 < M_D < 1.87 \text{ GeV}/c^2$ and $0.144 < \Delta M < 0.146 \text{ GeV}/c^2$. The large statistics of the sample makes it difficult for the model to fit data exactly, resulting in systematic deviations in the pull values from zero in the tails. Studies of MC samples have shown that the signal yield is unbiased and this systematic deviation in the pull values has negligible effect on the measured K_i and \bar{K}_i values. The efficiency- and migration-corrected yields are then used to determine the values of K_i and \bar{K}_i , which are given in table 4. The values of K_i and \bar{K}_i are in reasonable agreement with those reported in ref. [13]; the only deviation larger than 3σ is in bin 9, which contains only 1.2% of the data.

8 Determination of (x_\pm, y_\pm) from the $B^\pm \rightarrow Dh^\pm$ sample

We select both $B^+ \rightarrow DK^+$ and $B^+ \rightarrow D\pi^+$ decays because they have an identical topology, but the latter is less sensitive to CP -violation measurements because $r_B^{D\pi}$ is approximately twenty times smaller than r_B^{DK} . However, the $B^+ \rightarrow D\pi^+$ branching fraction is an order of magnitude larger than that of $B^+ \rightarrow DK^+$ and hence serves as an excellent calibration sample for the signal determination procedure. Furthermore, there is a significant background from $B^+ \rightarrow D\pi^+$ decays in the $B^+ \rightarrow DK^+$ sample from the misidentification of the charged pion as a kaon; a simultaneous fit to both samples allows this cross-feed to be directly determined from data.

The signal yield in each bin is obtained via a simultaneous two-dimensional fit to the nine D phase space bins with the data divided into $B^+ \rightarrow DK^+$, $B^- \rightarrow DK^-$, $B^+ \rightarrow D\pi^+$ and $B^- \rightarrow D\pi^-$ candidates, so there are 36 samples in total. The signal extraction is done

Bin no.	N_{D^0}	$N_{\bar{D}^0}$	K_i	\bar{K}_i
1	51048±282	50254±280	0.2229±0.0008	0.2249±0.0008
2	137245±535	58222±382	0.4410±0.0009	0.1871±0.0007
3	31027±297	105147±476	0.0954±0.0005	0.3481±0.0009
4	24203±280	16718±246	0.0726±0.0005	0.0478±0.0004
5	13517±220	20023±255	0.0371±0.0003	0.0611±0.0004
6	21278±269	20721±267	0.0672±0.0005	0.0679±0.0005
7	15784±221	13839±209	0.0403±0.0004	0.0394±0.0004
8	6270±148	7744±164	0.0165±0.0002	0.0183±0.0002
9	6849±193	6698±192	0.0070±0.0002	0.0054±0.0001

Table 4. D^0 and \bar{D}^0 yield in each bin of D phase space along with K_i and \bar{K}_i values measured in D^* tagged data sample.

by fitting ΔE and C_{NN} . The distribution of C_{NN} cannot be described readily by an analytic PDF. Therefore, we transform C_{NN} as

$$C'_{\text{NN}} = \log \left(\frac{C_{\text{NN}} - C_{\text{NN,low}}}{C_{\text{NN,high}} - C_{\text{NN}}} \right), \quad (8.1)$$

where $C_{\text{NN,low}} = -0.6$ and $C_{\text{NN,high}} = 0.9985$ are the minimum and maximum values of C_{NN} in the sample, respectively. The signal and background distributions of C'_{NN} can be described by combinations of Gaussian PDFs. The three background components considered are:

- *continuum* background from $e^+e^- \rightarrow q\bar{q}$ processes, where $q = (u, d, s, c)$
- *combinatorial $B\bar{B}$* background, in which the final state particles could be coming from both B mesons in an event; and
- *cross-feed peaking background from $B^+ \rightarrow Dh^+$* , where $h = \pi, K$, in which the charged kaon is misidentified as a pion or *vice versa*.

There is no significant correlation between ΔE and C'_{NN} , so the two-dimensional PDF for each of the components is the product of one-dimensional ΔE and C'_{NN} PDFs. The sum of a CB function and two Gaussian functions with a common mean is used as the PDF to model the ΔE signal component in both B samples. The sum of a Gaussian and an asymmetric Gaussian with different mean values is used to parametrize the PDF that describes the C'_{NN} signal component. The continuum background distribution is modeled with a first-order polynomial in ΔE and by the sum of two Gaussian PDFs with different mean values in C'_{NN} . The ΔE distribution of combinatorial $B\bar{B}$ background in $B^+ \rightarrow D\pi^+$ is described by an exponential function. There is a small peaking structure due to misreconstructed π^0 events, and this is modeled by a CB function. A first-order polynomial is added to the above two PDFs in the case of $B^+ \rightarrow DK^+$ decays. The C'_{NN} distribution

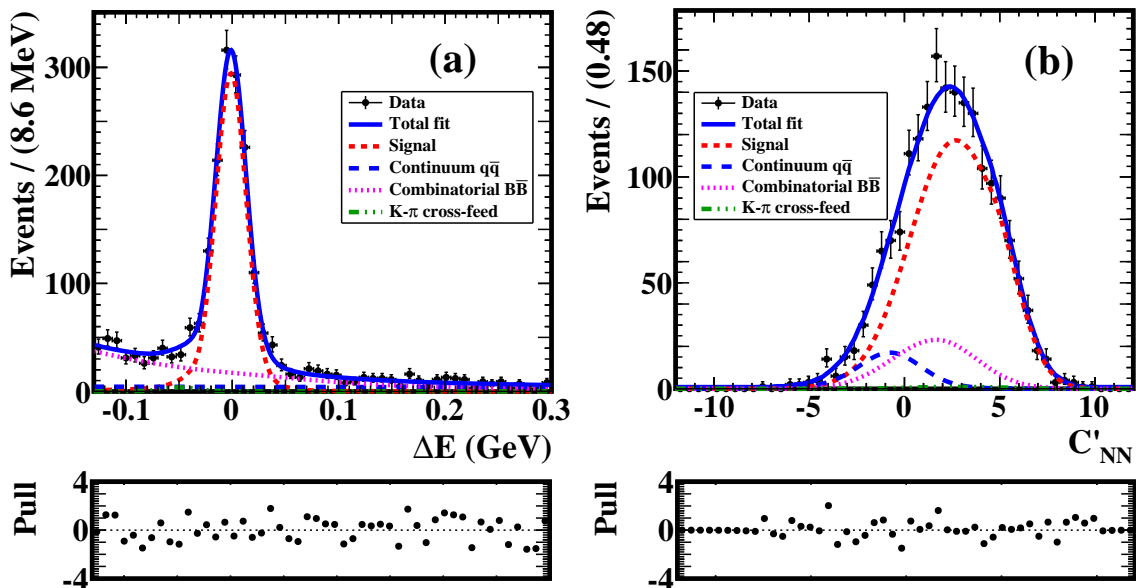


Figure 4. Signal-enhanced fit projections of (a) ΔE and (b) C'_{NN} for the $B^\pm \rightarrow D\pi^\pm$ data sample in bin 1. The black points with error bars are the data and the solid blue curves are the total fit. The dotted red, blue, magenta, and green curves represent the signal, continuum, combinatorial $B\bar{B}$ backgrounds and cross-feed peaking background components, respectively. The pull between the data and the fit is shown for both the projections.

for each of the samples is modeled by an asymmetric Gaussian function. The cross-feed peaking background in ΔE is modeled with the sum of three Gaussian functions, whereas the signal PDF itself is used for the C'_{NN} distribution.

All yields are determined from the fit to data. The signal mean value and polynomial parameter for continuum background ΔE distribution are determined from the fit to data, while all other shape parameters are fixed to those obtained from fits to appropriate MC samples. A scaling factor is applied on the ΔE signal resolution, which is a free parameter in the fit. All C'_{NN} parameters are fixed to the values obtained from MC. An additional shift is applied on the continuum background mean value as well as a scaling factor to the resolution. Both these parameters are determined from data, which ensures that any possible data-MC difference is taken into account. We do not perform an independent fit in each bin because the event yields become too small to determine all the free parameters. Therefore, common shape parameters are used for each bin except for the combinatorial $B\bar{B}$ background component in bin 1. A separate exponential parameter is used in bin 1 due to the difference in slope compared to other bins. These exponential parameters are also floated in the fit in addition to those mentioned earlier. The signal-enhanced fit projections for the data in bin 1 are shown in figure 4 and 5, where the signal regions are defined as $|\Delta E| < 0.05$ GeV and $C'_{\text{NN}} > 0$. The fitted signal yields are summarized in table 5. The total numbers of $B^\pm \rightarrow D\pi^\pm$ and $B^\pm \rightarrow DK^\pm$ signal events are 9981 ± 134 and 815 ± 51 , respectively.

The Cartesian parameters x_\pm and y_\pm are extracted from the simultaneous fit by ex-

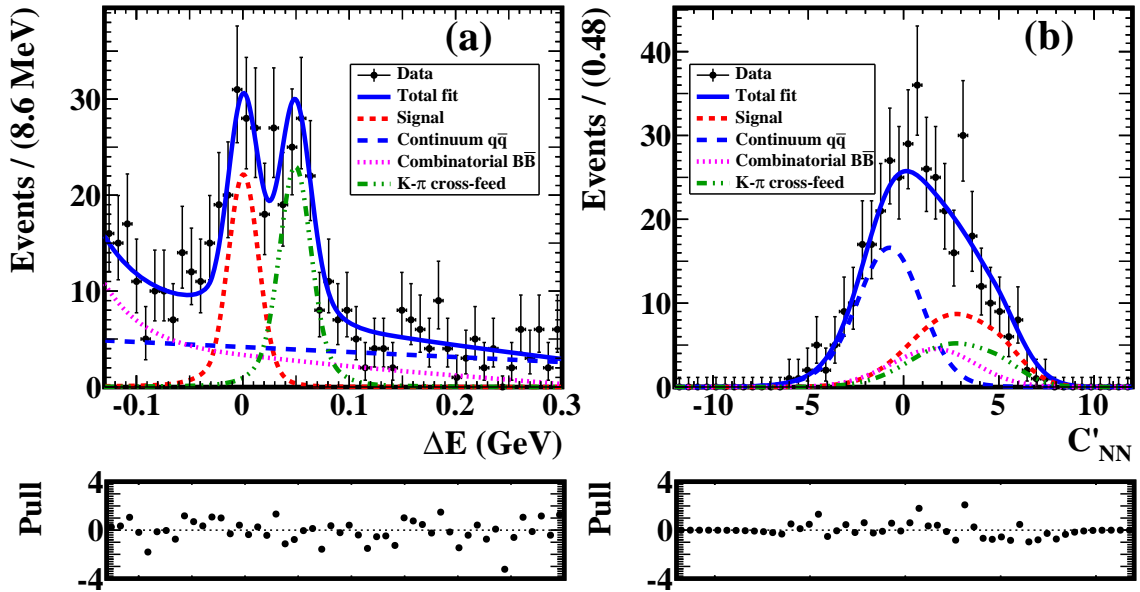


Figure 5. Signal-enhanced fit projections of (a) ΔE and (b) C'_{NN} for the $B^\pm \rightarrow DK^\pm$ data sample in bin 1. The black points with error bars are the data and the solid blue curves are the total fit. The dotted red, blue, magenta, and green curves represent the signal, continuum, combinatorial $B\bar{B}$ backgrounds and cross-feed peaking background components, respectively. The pull between the data and the fit is also shown for both the projections.

Bin no.	$B^\pm \rightarrow D\pi^\pm$		$B^\pm \rightarrow DK^\pm$	
	N_i^+	N_i^-	N_i^+	N_i^-
1	772 ± 33	860 ± 34	80 ± 13	58 ± 12
2	1077 ± 41	2088 ± 55	98 ± 16	190 ± 21
3	1639 ± 49	450 ± 28	121 ± 18	57 ± 13
4	263 ± 24	451 ± 29	21 ± 9	30 ± 11
5	377 ± 27	256 ± 23	23 ± 9	18 ± 9
6	338 ± 26	321 ± 26	35 ± 11	23 ± 9
7	253 ± 21	255 ± 22	16 ± 9	5 ± 7
8	154 ± 17	109 ± 15	9 ± 6	13 ± 7
9	162 ± 19	138 ± 19	21 ± 9	30 ± 10

Table 5. Signal yields in each D phase space bin for $B^\pm \rightarrow D\pi^\pm$ and $B^\pm \rightarrow DK^\pm$ data samples obtained from a simultaneous fit to the nine bins.

pressing the signal yield using eqs. (2.5) and (2.6); the procedure includes corrections for efficiency and migration between bins. The input parameters to the expressions in eqs. (2.5) and (2.6) include the values of K_i and \bar{K}_i obtained from the flavour-tagged D sample and the D strong-phase difference parameters c_i and s_i [13]. The results are summarized in table 6, and the statistical likelihood contours are shown in figure 6. The statistical cor-

	$B^\pm \rightarrow D\pi^\pm$				$B^\pm \rightarrow DK^\pm$			
x_+	0.039 ± 0.024	$+0.018$	$+0.014$	-0.013	-0.030 ± 0.121	$+0.017$	$+0.019$	-0.018
y_+	-0.196	$+0.080$	$+0.038$	$+0.032$	0.220	$+0.182$	± 0.032	$+0.072$
		-0.059	-0.034	-0.030		-0.541		-0.071
x_-	-0.014 ± 0.021	$+0.018$	$+0.019$	-0.010	0.095 ± 0.121	$+0.017$	$+0.023$	-0.016
		-0.010	-0.010			-0.016	-0.025	
y_-	-0.033 ± 0.059	$+0.018$	$+0.019$	-0.010	0.354	$+0.144$	$+0.015$	$+0.032$
		-0.019	-0.010			-0.197	-0.021	-0.049

Table 6. x_\pm and y_\pm parameters from a combined fit to $B^\pm \rightarrow D\pi^\pm$ and $B^\pm \rightarrow DK^\pm$ data samples. The first uncertainty is statistical, the second is systematic, and the third is due to the uncertainty on the c_i , s_i measurements.

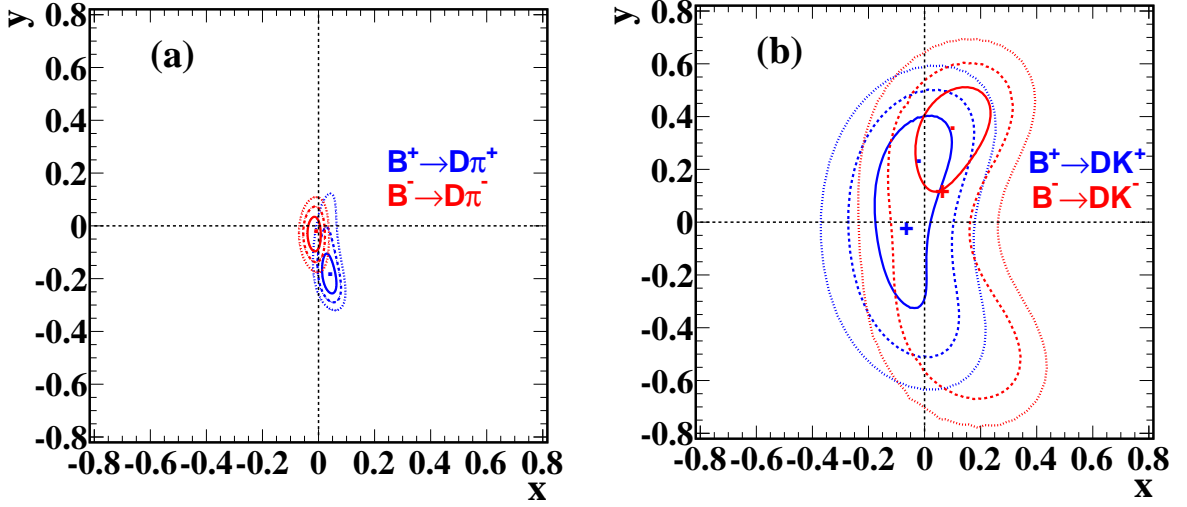


Figure 6. One (solid line), two (dashed line), and three (dotted line) standard deviation likelihood contours for the (x_\pm, y_\pm) parameters for (a) $B^\pm \rightarrow D\pi^\pm$ and (b) $B^\pm \rightarrow DK^\pm$ decays. The point marks the best fit value and the cross marks the expected value from the world average values of ϕ_3 , r_B^{DK} , and δ_B^{DK} [36].

	x_+	y_+	x_-	y_-
x_+	1	-0.364	0.314	0.050
y_+		1	0.347	0.055
x_-			1	-0.032
y_-				1

Table 7. Statistical correlation matrix for (x_+, y_+, x_-, y_-) measured from the $B^\pm \rightarrow D\pi^\pm$ data sample

relation matrices are given in tables 7 and 8. The measured and expected yields for the binned B^+ and B^- data are compared in figures 7 and 8.

	x_+	y_+	x_-	y_-
x_+	1	0.486	0.172	-0.231
y_+		1	-0.127	0.179
x_-			1	0.365
y_-				1

Table 8. Statistical correlation matrix for (x_+, y_+, x_-, y_-) measured from the $B^\pm \rightarrow DK^\pm$ data sample

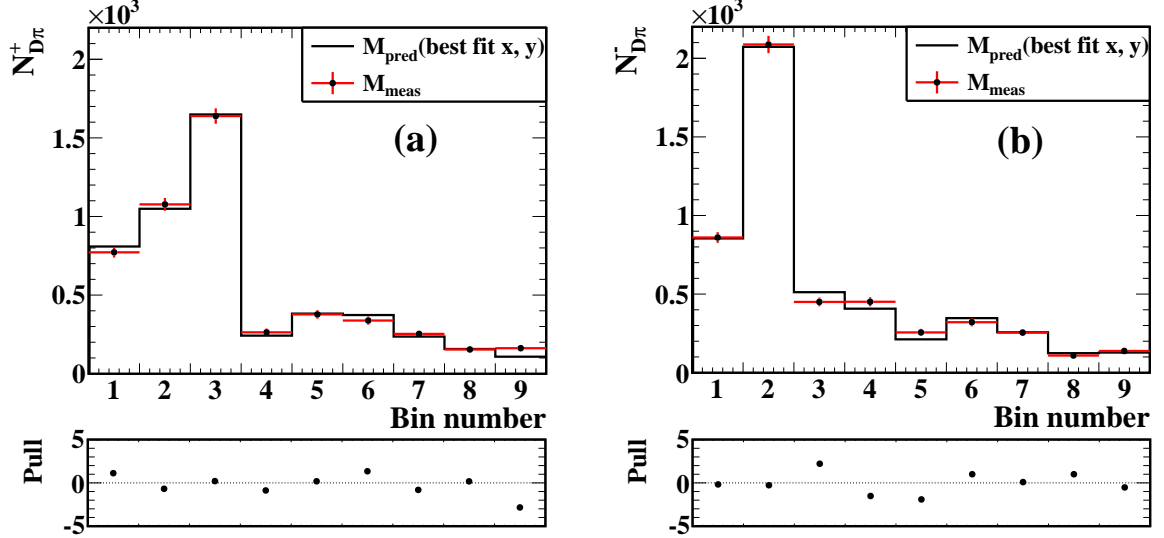


Figure 7. Measured and expected yields in bins for (a) $B^+ \rightarrow D\pi^+$ and (b) $B^- \rightarrow D\pi^-$ data samples. The data points with error bars are the measured yields, and the solid histogram is the expected yield from the best fit (x_\pm, y_\pm) parameter values.

9 Systematic uncertainties

We consider several possible sources of systematic uncertainty, as listed in table 9, along with their contributions. The remainder of this section describes how these uncertainties are estimated.

The limited size of the signal MC sample used for estimating the efficiency and the migration matrix is a source of systematic uncertainty. Efficiencies in B and D^* samples are varied by their statistical uncertainty ($\pm 1\sigma$) in each bin independently. The resultant negative and positive deviations in (x_\pm, y_\pm) are separately summed in quadrature. Similarly, the migration matrix elements are varied by their statistical uncertainty in B and D^* samples, one element at a time. The resultant positive and negative deviations are considered separately.

The systematic uncertainty due to the difference in mass resolution between data and the MC samples is considered by varying the width on the $\pi^+\pi^-\pi^0$ invariant mass distribution by the uncertainty on the resolution scale factor obtained in data, when compared

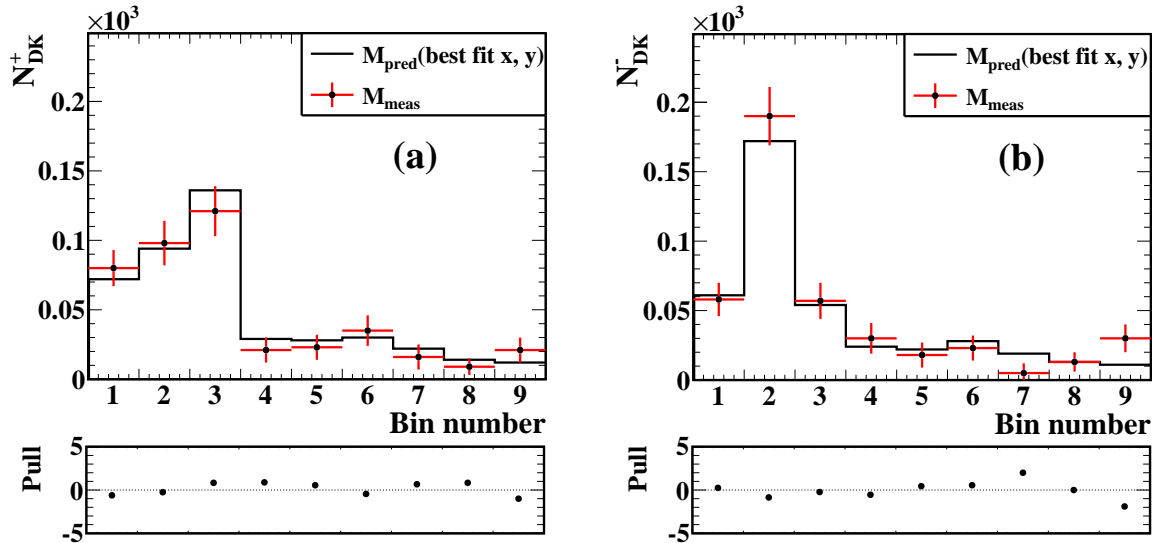


Figure 8. Measured and expected yields in bins for (a) $B^+ \rightarrow DK^+$ and (b) $B^- \rightarrow DK^-$ data samples. The data points with error bars are the measured yields, and the solid histogram is the expected yield from the best fit (x_{\pm}, y_{\pm}) parameter values.

to that in MC. The resultant deviations in (x_{\pm}, y_{\pm}) are taken as the systematic uncertainty from this source. All the other resonances are wide and the resolution difference is an order of magnitude smaller than the resolution, thus the modelling of resolution does not affect our measurements. The systematic effect of the uncertainty on the K_i and \bar{K}_i values is estimated by varying them by their statistical uncertainties independently. The resultant sum of deviations in quadrature is taken as the associated systematic uncertainty.

Modelling the data with PDFs that have parameters fixed to values obtained from MC samples is another source of systematic uncertainty. There are 14 signal and 23 background shape parameters fixed in the $B^{\pm} \rightarrow Dh^{\pm}$ simultaneous fit. These are fixed to the values obtained from MC samples. The uncertainty due to PDF modelling is taken into account by repeating the fit by individually varying the fixed parameters by $\pm 1\sigma$, where σ is the uncertainty on these parameters in MC component fits, and taking the difference in quadrature as the uncertainty. Any possible bias in the fit is studied with a set of pseudo-experiments with different input values for (x_{\pm}, y_{\pm}) . The fit is found to give an unbiased response within the statistical uncertainty from the finite number of pseudo-experiments, and this uncertainty is taken as the systematic uncertainty from this source.

The kaon identification efficiency and pion fake rate used in the fit are also fixed parameters that are determined from control samples of $D^{*+} \rightarrow D^0\pi^+$, $D^0 \rightarrow K^-\pi^+$. They are varied by $\pm 1\sigma$ and the resultant deviations in the nominal (x_{\pm}, y_{\pm}) values are assigned as the systematic uncertainty. The uncertainty on the c_i , s_i inputs reported in ref. [13] are also considered by varying c_i , s_i by their respective uncertainties and then considering the corresponding deviations in (x_{\pm}, y_{\pm}) from the nominal values as the systematic uncertainty. Here, the correlation between c_i , s_i is taken into account. The effect of the difference in the efficiency variation across the bins for B and D^* samples is studied. We find no deviation

Source	$B^\pm \rightarrow D\pi^\pm$				$B^\pm \rightarrow DK^\pm$			
	x_+	y_+	x_-	y_-	x_+	y_+	x_-	y_-
Efficiency	+0.013	+0.030	+0.012	+0.012	+0.012	+0.022	+0.012	+0.013
uncertainty	-0.009	-0.027	-0.008	-0.013	-0.013	-0.023	-0.012	-0.016
Migration matrix	+0.011	+0.021	+0.011	+0.013	+0.007	+0.015	+0.007	+0.006
uncertainty	-0.004	-0.019	-0.003	-0.014	-0.008	-0.016	-0.007	-0.012
$m_{\pi\pi^0}$ resolution	0.003	0.001	0.004	0.001	0.001	0.001	0.001	0.003
K_i, \bar{K}_i	+0.004	+0.007	+0.004	+0.002	+0.001	+0.001	+0.002	+0.001
uncertainty	-0.001	-0.006	-0.001	-0.002	-0.002	-0.001	-0.002	-0.001
PDF shape	+0.004	+0.004	+0.004	+0.001	+0.009	+0.017	+0.009	+0.001
	-0.008	-0.003	-0.004	-0.001	-0.008	-0.016	-0.007	-0.005
Fit bias	0.000	0.001	0.000	0.000	0.001	0.001	0.001	0.003
PID	0.001	0.001	0.001	0.000	0.002	0.001	0.002	0.001
Total systematic	+0.018	+0.038	+0.018	+0.018	+0.017	+0.032	+0.017	+0.015
uncertainty	-0.013	-0.034	-0.010	-0.019	-0.018	-0.032	-0.016	-0.021
c_i, s_i	+0.014	+0.032	+0.010	+0.019	+0.019	+0.072	+0.023	+0.032
uncertainty	-0.012	-0.030	-0.006	-0.010	-0.018	-0.071	-0.025	-0.049
Total statistical	+0.024	+0.080	+0.021	+0.059	+0.121	+0.182	+0.121	+0.144
uncertainty	-0.024	-0.059	-0.021	-0.059	-0.121	-0.541	-0.121	-0.197

Table 9. Systematic uncertainties from various sources in $B^\pm \rightarrow D\pi^\pm$ and $B^\pm \rightarrow DK^\pm$ data samples.

in K_i and \bar{K}_i values within their statistical uncertainty when the D^* efficiencies are varied by the maximum deviation found between the samples or D momentum range is changed to 1–3 GeV/ c .

10 Determination of ϕ_3 , r_B and δ_B

We use the frequentist treatment, which includes the Feldman-Cousins ordering [37], to obtain the physical parameters

$$\mu = (\phi_3, r_B, \delta_B),$$

from the measured parameters

$$z = (x_+, y_+, x_-, y_-),$$

in $B^\pm \rightarrow DK^\pm$ sample; this is the same procedure as was used in ref. [11]. We do not use the $B^\pm \rightarrow D\pi^\pm$ sample to constrain ϕ_3 , which has been the case in previous Belle analyses [11, 38]. We note that the constraints presented by the LHCb Collaboration [39] allow values up to $r_B^{D\pi} < 0.028$ at a 2σ confidence level, which is five times larger than the expectation; if the value of $r_B^{D\pi}$ is significantly larger than expected then future analyses

Parameter	Results	2σ interval
ϕ_3 ($^\circ$)	$5.7^{+10.2}_{-8.8} \pm 3.5 \pm 5.7$	(-29.7, 109.5)
δ_B ($^\circ$)	$83.4^{+18.3}_{-16.6} \pm 3.1 \pm 4.0$	(35.7, 175.0)
r_B	$0.323 \pm 0.147 \pm 0.023 \pm 0.051$	(0.031, 0.616)

Table 10. (ϕ_3, δ_B, r_B) obtained from the $B^\pm \rightarrow DK^\pm$ data sample. The first uncertainty is statistical, second is systematic and, the third one is due to the uncertainty on c_i, s_i measurements.

could include $B^\pm \rightarrow D\pi^\pm$ channel to determine ϕ_3 . The confidence level is calculated as

$$\alpha(\mu) = \frac{\int_{\mathcal{D}(\mu)} p(z|\mu) dz}{\int_{\infty} p(z|\mu) dz}, \quad (10.1)$$

where $p(z|\mu)$ is the probability density to observe the measurements z given the set of physical parameters μ . The integration domain $\mathcal{D}(\mu)$ is given by the likelihood ratio ordering in the Feldman-Cousins method. The PDF $p(z|\mu)$ is a multivariate Gaussian PDF with the uncertainties and correlations between (x_\pm, y_\pm) taken from the measurements.

We obtain the parameters $\mu = (\phi_3, r_B, \delta_B)$ from the fit as given in table 10. The systematic uncertainty is estimated by varying the z parameters by their corresponding systematic uncertainties. Figure 9 shows the confidence level contours representing one, two, and three standard deviations in (ϕ_3, r_B) and (ϕ_3, δ_B) planes.

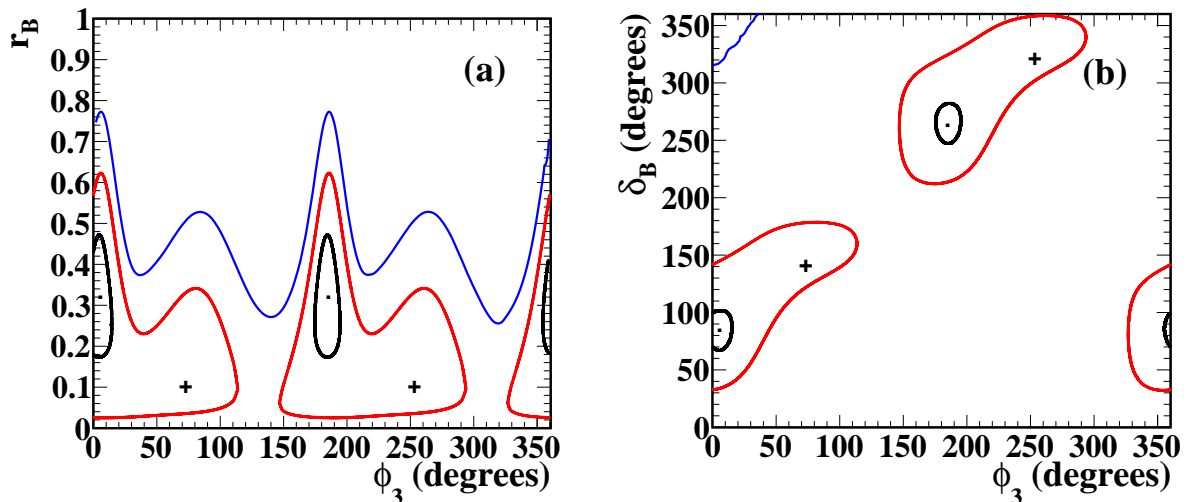


Figure 9. Projection of the statistical confidence intervals in the (a) $\phi_3 - r_B$ and (b) $\phi_3 - \delta_B$ planes. The black, red, and blue contours represent the one, two, and three standard deviation regions, respectively. The crosses show the positions of the world-average values [36].

We performed a check of the assumption that the (x_\pm, y_\pm) likelihood can be approximated to be Gaussian when using the Feldman-Cousins method to extract (ϕ_3, r_B, δ_B) . The check used the measured confidence intervals in (ϕ_3, r_B, δ_B) to generate an ensemble of simulated data sets. Each simulated data set was then fit to form a distribution of (x_\pm, y_\pm) ,

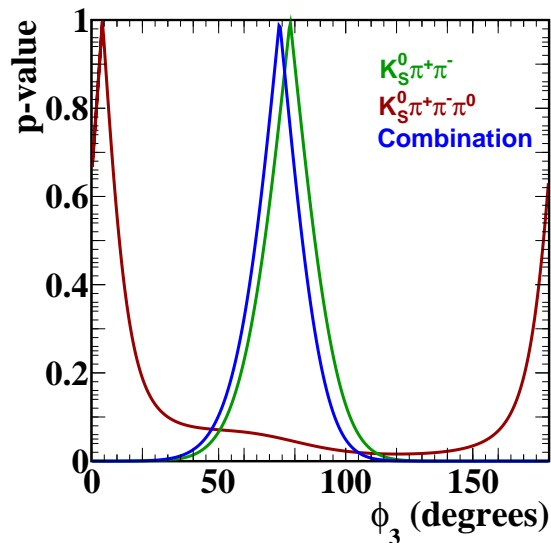


Figure 10. Distribution of p-value for ϕ_3 from multibody D final states at Belle, which is shown by the solid blue curve. The results from $B \rightarrow DK^{(*)}$ decays with $D \rightarrow K_S^0 \pi^+ \pi^-$ are shown by the solid green curve and the $D \rightarrow K_S^0 \pi^+ \pi^- \pi^0$ final states are shown by the solid brown curve [11, 38].

which was found to be consistent with the (x_{\pm}, y_{\pm}) confidence intervals measured. Hence we conclude that the reported confidence intervals for (ϕ_3, r_B, δ_B) are appropriate.

There is a two-fold ambiguity in ϕ_3 and δ_B results with $\phi_3 + 180^\circ$ and $\delta_B + 180^\circ$. We choose the solution that satisfies $0^\circ < \phi_3 < 180^\circ$. This result includes the current world-average value [36] within two standard deviations. We observe that there is a local minimum of the likelihood around $\phi_3 = 75^\circ$ and $\delta_B = 155^\circ$.

We combine the results presented here with the model-independent $B^+ \rightarrow D(K_S^0 \pi^+ \pi^-)K^+$ [11] and $B^0 \rightarrow D^0(K_S^0 \pi^+ \pi^-)K^{*0}$ [38] results from Belle. Without our measurement, the combination leads to $\phi_3 = (78_{-15}^{+14})^\circ$. Including our measurement, the combination gives $\phi_3 = (74_{-14}^{+13})^\circ$. The distributions of p-values for the ϕ_3 measurements from the individual D final states and the combination are given in figure 10. The separate measurements and the combination likelihood contours in the (ϕ_3, r_B) plane are shown in figure 11.

11 Conclusion

We have performed the first measurement of the unitarity triangle angle ϕ_3 using a model-independent analysis of $B^+ \rightarrow D(K_S^0 \pi^+ \pi^- \pi^0)K^+$ decays using the full data sample collected by the Belle detector, which corresponds to $772 \times 10^6 B\bar{B}$ events. The D strong-phase difference measurements for $D \rightarrow K_S^0 \pi^+ \pi^- \pi^0$ [13] are used as external inputs to the analysis. The result obtained is $\phi_3 = (5.7_{-8.8}^{+10.2} \pm 3.5 \pm 5.7)^\circ$. The first uncertainty is statistical, the second is systematic, and the third is due to the uncertainty on the c_i and s_i measurements. The ratio of the suppressed and favoured amplitudes is $r_B = 0.323 \pm 0.147 \pm 0.023 \pm 0.051$.

This measurement can be improved upon once a suitable amplitude model for $D^0 \rightarrow K_S^0 \pi^+ \pi^- \pi^0$ is available to provide guidance in choosing a more sensitive binning. Fur-

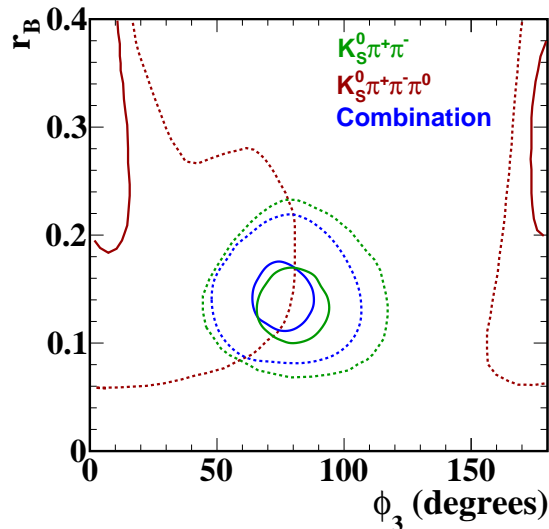


Figure 11. Projections of the confidence contours in the $\phi_3 - r_B$ plane from multibody D final states at Belle, which is shown by the blue contours. The results from $B \rightarrow DK^{(*)}$ decays with $D \rightarrow K_S^0 \pi^+ \pi^-$ are shown by the green contours and the $D \rightarrow K_S^0 \pi^+ \pi^- \pi^0$ final states are shown by the brown contours. The solid and dashed curves correspond to one and two standard deviation contours, respectively [11, 38].

thermore, the larger sample of $e^+e^- \rightarrow \psi(3770)$ data that has been collected by BESIII will determine c_i and s_i more precisely, thus reducing the systematic uncertainty. The results presented here, combined with the improvements in binning and the increased sample of B decays that will be available at Belle II, mean that model-independent analysis of $B^+ \rightarrow D(K_S^0 \pi^+ \pi^- \pi^0)K^+$ is a very promising addition to the suite of modes to be used to determine ϕ_3 to a precision of $1\text{--}2^\circ$ [40].

Acknowledgments

We thank the KEKB group for the excellent operation of the accelerator; the KEK cryogenics group for the efficient operation of the solenoid; and the KEK computer group, and the Pacific Northwest National Laboratory (PNNL) Environmental Molecular Sciences Laboratory (EMSL) computing group for strong computing support; and the National Institute of Informatics, and Science Information NETwork 5 (SINET5) for valuable network support. We acknowledge support from the Ministry of Education, Culture, Sports, Science, and Technology (MEXT) of Japan, the Japan Society for the Promotion of Science (JSPS), and the Tau-Lepton Physics Research Center of Nagoya University; the Australian Research Council including grants DP180102629, DP170102389, DP170102204, DP150103061, FT130100303; Austrian Science Fund (FWF); the National Natural Science Foundation of China under Contracts No. 11435013, No. 11475187, No. 11521505, No. 11575017, No. 11675166, No. 11705209; Key Research Program of Frontier Sciences, Chinese Academy of Sciences (CAS), Grant No. QYZDJ-SSW-SLH011; the CAS Center for Excellence in Particle Physics (CCEPP); the Shanghai Pujiang Program under Grant

Bin	ϵ (%)					
	$D^{*+} \rightarrow D^0 \pi^+$	$D^{*-} \rightarrow \bar{D}^0 \pi^-$	$B^+ \rightarrow DK^+$	$B^- \rightarrow DK^-$	$B^+ \rightarrow D\pi^+$	$B^- \rightarrow D\pi^-$
1	3.07 ± 0.06	3.02 ± 0.06	3.77 ± 0.05	3.84 ± 0.05	4.43 ± 0.06	4.35 ± 0.06
2	3.77 ± 0.05	4.83 ± 0.09	5.44 ± 0.07	5.01 ± 0.04	6.15 ± 0.08	5.47 ± 0.04
3	5.66 ± 0.14	3.66 ± 0.05	4.97 ± 0.04	4.88 ± 0.10	5.55 ± 0.05	5.55 ± 0.10
4	3.60 ± 0.11	3.72 ± 0.12	4.55 ± 0.10	4.63 ± 0.09	5.29 ± 0.11	5.17 ± 0.09
5	3.77 ± 0.14	3.38 ± 0.11	4.89 ± 0.10	4.28 ± 0.10	5.47 ± 0.10	4.53 ± 0.11
6	3.71 ± 0.11	3.45 ± 0.11	4.68 ± 0.09	4.28 ± 0.09	5.46 ± 0.10	5.04 ± 0.09
7	3.87 ± 0.17	4.03 ± 0.19	4.92 ± 0.16	4.66 ± 0.14	5.64 ± 0.18	5.29 ± 0.14
8	3.36 ± 0.24	3.53 ± 0.21	5.36 ± 0.19	4.77 ± 0.20	5.75 ± 0.20	5.56 ± 0.22
9	3.32 ± 0.16	3.21 ± 0.16	4.64 ± 0.14	4.21 ± 0.13	4.87 ± 0.15	4.83 ± 0.14

Table 11. Efficiency in each bin of the D phase space for $D^{*\pm} \rightarrow D\pi^\pm$, $B^\pm \rightarrow DK^\pm$, and $B^\pm \rightarrow D\pi^\pm$ decays determined from the corresponding signal MC samples.

No. 18PJ1401000; the Ministry of Education, Youth and Sports of the Czech Republic under Contract No. LTT17020; the Carl Zeiss Foundation, the Deutsche Forschungsgemeinschaft, the Excellence Cluster Universe, and the VolkswagenStiftung; the Department of Science and Technology of India; the Istituto Nazionale di Fisica Nucleare of Italy; National Research Foundation (NRF) of Korea Grants No. 2016R1D1A1B01010135, No. 2016R1D1A1B02012900, No. 2018R1A2B3003643, No. 2018R1A6A1A06024970, No. 2018R1D1A1B07047294, No. 2019K1A3A7A09033840; Radiation Science Research Institute, Foreign Large-size Research Facility Application Supporting project, the Global Science Experimental Data Hub Center of the Korea Institute of Science and Technology Information and KREONET/GLORIAD; the Polish Ministry of Science and Higher Education and the National Science Center; the Grant of the Russian Federation Government, Agreement No. 14.W03.31.0026; the Slovenian Research Agency; Ikerbasque, Basque Foundation for Science, Spain; the Swiss National Science Foundation; the Ministry of Education and the Ministry of Science and Technology of Taiwan; and the United States Department of Energy and the National Science Foundation.

A Efficiency and Migration matrix

The efficiencies in nine bins of D phase space in $D^{*\pm} \rightarrow D\pi^\pm$, $B^\pm \rightarrow DK^\pm$ and $B^\pm \rightarrow D\pi^\pm$ decays determined from signal MC samples are given in table 11. The migration matrices for $B^+ \rightarrow DK^+$ and $B^+ \rightarrow D\pi^+$ decays estimated from signal MC samples are given in tables 12 and 13, respectively.

References

- [1] N. Cabibbo, *Unitary symmetry and leptonic decays*, *Phys. Rev. Lett.* **10**, (1963) 531.

Bin no.	1	2	3	4	5	6	7	8	9
1	0.93	0.01	0.01	0.01	0.01	0.01	0.00	0.00	0.01
2	0.01	0.96	0.02	0.00	0.00	0.00	0.00	0.00	0.00
3	0.01	0.02	0.95	0.00	0.00	0.00	0.00	0.00	0.00
4	0.04	0.03	0.02	0.90	0.00	0.00	0.00	0.00	0.01
5	0.04	0.01	0.03	0.01	0.91	0.01	0.00	0.00	0.01
6	0.02	0.02	0.01	0.01	0.01	0.92	0.01	0.00	0.00
7	0.01	0.03	0.02	0.00	0.01	0.02	0.91	0.00	0.01
8	0.01	0.02	0.02	0.01	0.00	0.01	0.01	0.88	0.02
9	0.06	0.02	0.02	0.01	0.01	0.01	0.01	0.00	0.86

Table 12. Migration matrix for $B^+ \rightarrow DK^+$ decays estimated from the signal MC sample. The rows correspond to the true bins and columns show the reconstructed bins.

Bin no.	1	2	3	4	5	6	7	8	9
1	0.93	0.01	0.01	0.01	0.01	0.01	0.00	0.00	0.01
2	0.01	0.96	0.01	0.00	0.00	0.00	0.00	0.00	0.00
3	0.01	0.02	0.95	0.01	0.00	0.01	0.00	0.00	0.00
4	0.03	0.02	0.02	0.92	0.00	0.01	0.00	0.00	0.00
5	0.03	0.02	0.02	0.01	0.91	0.01	0.00	0.00	0.01
6	0.03	0.02	0.01	0.01	0.00	0.93	0.00	0.01	0.00
7	0.01	0.03	0.01	0.00	0.00	0.01	0.92	0.00	0.01
8	0.00	0.01	0.03	0.00	0.01	0.01	0.01	0.92	0.01
9	0.05	0.01	0.01	0.01	0.00	0.02	0.01	0.01	0.88

Table 13. Migration matrix for $B^+ \rightarrow D\pi^+$ decays estimated from the signal MC sample. The rows correspond to the true bins and columns show the reconstructed bins.

- [2] M. Kobayashi and T. Maskawa, *CP violation in the renormalizable theory of weak interaction*, *Prog. Theor. Phys.* **49**, (1973) 652.
- [3] J. Brod and J. Zupan, *The ultimate theoretical error on γ from $B \rightarrow DK$ decays*, *J. High Energ. Phys.* **01**, 051 (2014).
- [4] CKMfitter Group, J. Charles et al., *CP Violation and the CKM Matrix: Assessing the Impact of the Asymmetric B factories*, *Eur. Phys. J. C* **41**, (2005) 1-131, [hep-ph/0406184], updated results and plots available at:<http://ckmfitter.in2p3.fr>
- [5] M. Blanke and A. Buras, *Emerging ΔM_d - anomaly from tree-level determinations of $|V_{cb}|$ and the angle γ* , *Eur. Phys. J. C* **79**, (2019) 159.
- [6] J. Brod, A. Lenz, G. Tetlalmatzi-Xolocotzi, and M. Wiebusch *New physics effects in tree-level decays and the precision in the determination of the quark mixing angle γ* , *Phys. Rev. D* **92**, (2015) 033002.

- [7] LHCb Collaboration, R. Aaij et al., *Measurement of the CKM angle γ using $B^\pm \rightarrow DK^\pm$ with $D \rightarrow K_S^0 \pi^+ \pi^-$, $K_S^0 K^+ K^-$ decays*, *J. High Energy. Phys.* **1808** (2018) 176; Erratum [JHEP **1810** (2018) 107].
- [8] A. Giri, Yu. Grossman, A. Soffer, and J. Zupan, *Determining γ using $B^\pm \rightarrow DK^\pm$ with multibody D decays*, *Phys. Rev. D* **68**, (2003) 054018, [hep-ph/0303187].
- [9] A. Bondar, *Proceedings of BINP special analysis meeting on Dalitz analysis*, 2002 (unpublished).
- [10] CLEO Collaboration, J. Libby et al., *Model-independent determination of the strong-phase difference between D^0 and $\bar{D}^0 \rightarrow K_{S,L}^0 h^+ h^-$ ($h = \pi, K$) and its impact on the measurement of the CKM angle γ/ϕ_3* , *Phys. Rev. D* **82** (2010) 112006, [arXiv:1010.2817 hep-ex].
- [11] Belle Collaboration, H. Aihara et al., *First measurement of ϕ_3 with a model-independent Dalitz plot analysis of $B^\pm \rightarrow DK^\pm$, $D \rightarrow K_S^0 \pi^+ \pi^-$ decay*, *Phys. Rev. D* **85**, (2012) 112014, [arXiv:1204.6561 hep-ex].
- [12] Particle Data Group, M. Tanabashi et al., *Review of Particle Physics*, *Phys. Rev. D* **98**, (2018) 030001.
- [13] P. K. Resmi, J. Libby, S. Malde, and G. Wilkinson, *Quantum-correlated measurements of $D \rightarrow K_S^0 \pi^+ \pi^- \pi^0$ decays and consequences for the determination of the CKM angle γ* , *J. High Energy. Phys.* **01**, (2018) 82, [arXiv:1710.10086 hep-ex].
- [14] Y. Kubota et al., *The CLEO II detector*, *Nucl. Instrum. Meth. A* **320**, (1992) 66.
- [15] D. Peterson et al., *The CLEO III detector*, *Nucl. Instrum. Meth. A* **478**, (2002) 142.
- [16] M. Artuso et al., *Construction, pattern recognition and performance of the CLEO III LiF-TEA RICH detector*, *Nucl. Instrum. Meth. A* **502**, (2003) 91.
- [17] CLEO-c/CESR-c Taskforces and CLEO-c Collaboration, R. A. Briere et al., *CLEO-c and CESR-c: a new frontier of weak and strong interactions*, *Cornell LEPP Report CLNS Report No. 01/1742* (2001).
- [18] Belle Collaboration, A. Poluektov et al., *Evidence for direct CP violation in the decay $B^\pm \rightarrow D^{(*)} K^\pm$, $D \rightarrow K_S^0 \pi^+ \pi^-$ and measurement of the CKM phase ϕ_3* , *Phys. Rev. D* **81**, (2010) 112002, [arXiv:1003.3360 hep-ex].
- [19] D. J. Lange, *The EvtGen particle decay simulation package*, *Nucl. Instrum. Meth. A* **462**, (2001) 152.
- [20] R. Brun et al., *GEANT 3.21, CERN Program Library Long Writeup W5013* (unpublished).
- [21] E. Barberio and Z. Was, *PHOTOS - a universal Monte Carlo for QED radioactive corrections: version 2.0*, *Comput. Phys. Commun.* **79**, (1994) 291.
- [22] Belle Collaboration, A. Abashian et al., *The Belle Detector*, *Nucl. Instrum. Methods Phys. Res. A* **479**, (2002) 117, [arXiv:1710.10086 hep-ex].
- [23] Belle Collaboration, J. Brodzicka et al., *Physics Achievements from the Belle Experiment*, *Prog. Theor. Exp. Phys.* **2012**, (2012) 04D001, [arXiv:1212.5342 hep-ex].
- [24] S. Kurokawa and E. Kikutani, *Overview of the KEKB accelerators*, *Nucl. Instr. and Meth. A* **499**, (2003) 1, and other papers included in this volume.
- [25] T. Abe et al., *Achievements of KEKB*, *Prog. Theor. Exp. Phys.* **2013**, (2013) 03A001 and references therein.

- [26] M. Kenzie, M. Martinelli and N. Tuning, *Estimating $r_B^{D\pi}$ as an input to the determination of the CKM angle γ* , *Phys. Rev. D* **94**, (2016) 054021, [arXiv:1606.09129 hep-ph].
- [27] Belle Collaboration, Y. Horii et al., *Evidence for the Suppressed Decay $B^- \rightarrow DK^-$, $D \rightarrow K^+\pi^-$* , *Phys. Rev. Lett.* **106**, (2011) 231803, [arXiv:1103.5951 hep-ex].
- [28] M. Feindt and U. Kerzel, *The NeuroBayes neural network package*, *Nucl. Instrum. Methods Phys. Res. A* **559**, (2006) 190.
- [29] H. Nakano, *Search for new physics by a time-dependent CP violation analysis of the decay $B \rightarrow K_S \eta \gamma$ using the Belle detector*, Ph.D. Thesis, Tohoku University, 2014, Chap. 4 (unpublished), <https://belle.kek.jp/belle/theses/doctor/nakano15.pdf>.
- [30] R. A. Fisher, *Observables for the analysis of event shapes in e^+e^- annihilation and other processes*, *Annals of Eugenics* **7**, (1936) 179.
- [31] G. C. Fox and S. Wolfram, *Observables for the analysis of event shapes in e^+e^- annihilation and other processes*, *Phys. Rev. Lett.* **41**, (1978) 1581.
- [32] Belle Collaboration, S. H. Lee et al., *Evidence for $B^0 \rightarrow \pi^0\pi^0$* , *Phys. Rev. Lett.* **91**, (2003) 261801.
- [33] H. Tajima et al., *Proper time resolution function for measurement of time evolution of B mesons at the KEK B factory*, *Nucl. Instrum. Meth. A* **533**, (2004) 370, [arXiv:0301026 hep-ex].
- [34] H. Kakuno et al., *Neutral B Flavor Tagging for the Measurement of Mixing-induced CP Violation at Belle*, *Nucl. Instrum. Meth. A* **533**, (2004) 516, [arXiv:0403022 hep-ex].
- [35] T. Skwarnicki, *A study of the radiative cascade transitions between the Υ and Υ' resonances*, *Ph.D. Thesis (Appendix E)*, DESY F31-86-02 (1986).
- [36] Heavy Flavor Averaging Group, Y. Amhis et al., *Averages of b-hadron, c-hadron and τ -lepton properties as of November 2016*, *Eur. Phys. J C* **77**, (2017) 895, [arXiv:1612.07233 hep-ex].
- [37] G. J. Feldman and R. D. Cousins, *Unified approach to the classical statistical analysis of small signals*, *Phys. Rev. D* **57**, (1998) 3873.
- [38] Belle Collaboration, K. Negishi et al., *First model-independent Dalitz analysis of $B^0 \rightarrow DK^{*0}$, $D \rightarrow K_S^0\pi^+\pi^-$ decay*, *Prog. Theor. Exp. Phys.* **2016**, (2016) 043C01.
- [39] LHCb Collaboration, R. Aaij et al. *Measurement of the CKM angle γ from a combination of LHCb results*, *J. High Energ. Phys.* **12**, (2016) 087.
- [40] Belle II Collaboration, B2TiP theory community, and E. Kou et al., *The Belle II Physics Book*, (2018) [arXiv:1808.10567 hep-ex].